

Structural, Opto-electronic, Light sensing & Photocatalytic properties of CuO/Cu₂O Composite and Transition metal modified CuO

M.Sc. Thesis

By

RACHIT DOBHAL



DISCIPLINE OF PHYSICS
INDIAN INSTITUTE OF TECHNOLOGY INDORE
JUNE 2021

**Structural, Opto-electronic, Light sensing & Photocatalytic properties of CuO/Cu₂O Composite and
Transition metal modified CuO**

A THESIS

*Submitted in partial fulfillment of the
requirements for the award of the degree*

of

Master of Science

by

RACHIT DOBHAL



**DISCIPLINE OF PHYSICS
INDIAN INSTITUTE OF TECHNOLOGY INDORE
JUNE 2021**



INDIAN INSTITUTE OF TECHNOLOGY INDORE

CANDIDATE'S DECLARATION

I hereby certify that the work which is being presented in the thesis entitled Structural, Opto-electronic, Light sensing & Photocatalytic properties of CuO/Cu₂O Composite and Transition metal modified CuO in the partial fulfillment of the requirements for the award of the degree of **MASTER OF SCIENCE** and submitted in the **DISCIPLINE OF PHYSICS, Indian Institute of Technology Indore**, is an authentic record of my own work carried out during the time period from July 2019 to June 2021 under the supervision of Dr. Somaditya Sen, Associate Professor, Discipline Physics, Indian Institute of Technology Indore. The matter presented in this thesis has not been submitted by me for the award of any other degree of this or any other institute.

Rachit Dobhal
14/06/2020

**Signature of the student with date
(RACHIT DOBHAL)**

Signature(s) of Supervisor(s) of MSc thesis

Date: 19th June 2021

This is to certify that the above statement made by the candidate is correct to the best of my/our knowledge.

RACHIT DOBHAL has successfully given his M.Sc. Oral Examination held on 19th June 2021.



Signature(s) of Supervisor(s) of MSc thesis

Date: 19th June 2021



24-06-2021

Convener, DPGC

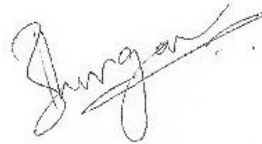
Date:



Signature of PSPC Member #1

(Dr. Sudip Chakraborty)

Date: 24/06/2021



Signature of PSPC Member #2

(Dr. Bhargav Vaidya)

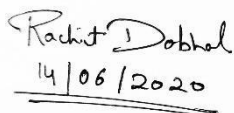
Date: 24/06/2021

ACKNOWLEDGEMENT

First and foremost, I would like to express my sincere and innermost sense of gratitude to Dr. Somaditya Sen (Associate Professor, Discipline of Physics, IIT Indore) for his guidance during my M.Sc. tenure. I sincerely acknowledge him for providing me all the opportunities and motivations throughout my graduate studies. Special thanks to his encouragement at times of loss and despair. I acknowledge his assistance in helping and encouraging me during this pandemic situation to work and focus, which has broadened my research horizon.

I express my deepest gratefulness to my PSPC members Dr. Sudip Chakraborty (Associate Professor, Discipline of Physics, IIT Indore) and Dr. Bhargav Vaidya (Associate Professor, DAASE IIT- INDORE) for their valuable questions, insightful comments, and motivation.

I sincerely thank Sir and DST-Women Scientist Dr. EG Rini for motivating me throughout the course work. A special thanks to Ph.D. seniors Mr. Prashant Kumar Mishra, Mr. Vishesh Manjunath for being so helpful and motivating and helping me deal with & have helped me in every aspect of my research life. I sincerely express gratitude to them.



Rachit Dobhal
14/06/2020

Date: - 19th June 2021

Rachit Dobhal

Dedicated to

My Parents, Teachers

&

All Well Wishers

TABLE OF CONTENTS-

CANDIDATE'S DECLARATION

ACKNOWLEDGEMENTS

LIST OF FIGURES

ABBREVIATIONS

Chapter 1- Introduction-

1.1 Crystal structure and constants

1.1.1 CuO

1.1.2 - Cu₂O

1.2 Fundamental Properties and Application

1.2.1-Sensing Applications-

1.2.2 - solar energy conversion-

1.2.3 -Photocatalytic activity:

1.3 - Literature Survey:

Chapter 2-- Experimental Details

2.1 - Synthesis Process

2.1.1 - Chelation-

2.1.2 - Aging and Drying-

2.2 Synthesis of samples

2.2.1 - Synthesis of CuO/Cu₂O Composite-

2.2.2 - Synthesis of Fe -Doped CuO

2.2.3 - Synthesis of Ti Doped CuO-

2.3 - Experimental Techniques Used-

2.3.1 - X-Ray Diffraction

2.3.1.1 - Principle and parts

2.3.1.2 System specifications:

2.3.2-Field emission scanning electron spectroscopy

2.3.2.1 -X-ray generation is a two-step process in FESEM.

2.3.3 - UV-Vis Absorption Spectroscopy-

2.3.3.1 Instrumentation

2.3.4 - Set up for UV and Visible Light sensing:

2.4 - Rietveld Refinement-

Chapter 3

3.1 - Structural properties-

3.1.1 - Phase-detection of CuO/Cu₂O composite -

3.1.2 - Effect on Fe Doping in CuO-

3.1.3 - Effect on Ti Doping in CuO-

Chapter 4 -Optical properties of Composite CuO/Cu₂O and Fe, Ti- Doped CuO

4.1- Bandgap Analysis-

4.2 - The Urbach Energy

4.2.1 Origin of Urbach tail-

4.3 - CuO-Cu₂O-

4.4 - Fe-doped CuO

4.5 - Ti Doped CuO-

Chapter 5- Electrical and Light sensing properties of CuO/Cu₂O and Fe, Ti-doped CuO.

5.1 - Proposed Model and Principle

5.2 - UV and Visible light sensing of CuO/Cu₂O-

5.3 - Fe-doped CuO-

5.4 - Ti Doped CuO-

Chapter 6

6.1 – Photocatalysis of Composite CuO/Cu₂O-

Chapter 7 Conclusion and future work-

List of Figures-

Figure 1 CuO Unit Cell (Red ball "Cu," Yellow ball" O "

Figure 2 Cu₂O Unit Cell

Figure 3 Cu₂O FCC and BCC unit cells

Figure 4 Electron Hole pair generation under UV illumination by nanoparticle

Figure 5 Sol-Gel method

Figure 6 Characteristic X-ray generation

Figure 7 Bragg's diffraction

Figure 8 Schematic diagram of Field Emission Scanning Electron Microscope

Figure 9 Schematic of Specular and Diffuse reflection

Figure 10 Schematic diagram of the UV-Vis spectrometer

Figure 11 a schematic diagram for the UV to Visible light-sensing setup along with photographs of the different wavelengths of light

Figure 12 Rietveld Refined Pure CuO

Figure 13 XRD S250, S500

Figure 14 a- XRD Fe Doped CuO, b- Lattice Parameters, c- Crystallite size and Lattice Strain, d-bond length, bond angle.

Figure 15 XRD, Bond Angle and Lattice Parameter of Ti-doped CuO.

Figure 16 localized state formation in between the valance band and Conduction band.

Figure 17 a Direct band Gap; b- Indirect bandgap of S250 and S500

Figure 18 a- Tauc Plot, b-Band Gap and Urbach Energy of Fe Doped CuO

Figure 19 a- E_g , E_u plots; b- Tau Plot Of Ti-doped CuO.

Figure 20 a-UV Sensing of S250, S500; b-Visible Sensing of S50; c- Current Constant (UV), d- Time Constant (UV)
; d- Current and Time Constant of S500 Visible Sensing

Figure 21 a-UV sensing; b- Current and Time Constant, of Fe Doped CuO

Abbreviations (if any)

Bandgap	E_g
Urbach Energy	EU
Oxygen Vacancies	V_o
Copper Vacancies	V_{Cu}
Oxygen Interstitial	Oi
Ultraviolet	UV
Visible	Vis
Diffuse reflectance spectroscopy	DRS
Methylene Blue Dye	MB
X-ray Diffraction	XRD

Chapter 1

Introduction-

The synthesis of nanoparticles (NPs) is currently a hot topic in science due to its unique electrical, magnetic, optical, and catalytic properties¹. Compared to typical and commercial bulk materials, this makes them attractive candidates for biological, optical, and electrical applications. Metallic nanoparticles also have lower melting temperatures, a higher specific surface area, better mechanical strength, and superior optical and magnetic characteristics than bulk metals. Metal oxide NPs, as a result, play an important role in chemistry, physics, and material science². Transition metal oxides are semiconductors with scientific and industrial applications in the magnetic storage medium, solar energy conversion, electronics, and catalysis. Furthermore, metal oxides with multivalent oxidation states drew a lot of attention from specialists because of their wide range of interesting and unique qualities, such as nontoxicity, environmental friendliness, and long-term stability.³

Transition metal oxides such as NiO, ZnO, TiO₂, Fe₂O₃, and CuO used in magnetic storage media, resonance imaging, bio separation, medicine, and wastewater treatment have recently received greater attention⁴. TiO₂ is used as a pigment in paints, toothpaste, and ointments⁵. Because ZnO and TiO₂ NPs are transparent, they are employed as sunscreens to improve the effectiveness and use of products⁶. Socks, shirts, and paints contain silver nanoparticles with antibacterial characteristics. As a result, nanoparticles are found in a wide variety of daily consumer goods. Copper oxide (CuO) NPs are one of the most important metal oxide NPs that have attracted attention due to their low cost, plentiful availability, good stability, and simple manufacturing procedure, among other factors that make them appealing for a variety of applications⁷. CuO NPs, as a result, have better electrical and optical characteristics than their bulk counterparts⁸.

1.1 Crystal Structure and Some Physics Constants

1.1.1 CuO-

CuO crystals have a monoclinic shape with symmetry $c2/c$ ⁹. Per unit cell, cupric oxide has four formula units. A copper atom has a coordination number of 4, indicating that it is coupled to four oxygen neighbor atoms in a roughly square planar arrangement (110) plane. A significant Jahn-Teller effect distorts divalent copper surrounds in all crystalline solids, resulting in more stable square planar groups. In this plane, the Cu-O bond lengths are 1.95 and 1.96 Å, respectively, longer than in cuprous oxide. The following two Cu-O bond lengths perpendicular to the aircraft are significantly longer, ruling out an octahedral kind of coordination. In the form of a distorted tetrahedron,

the O atom is coordinated into four Cu atoms. Even though the oxidation state of Cu in CuO is indisputably Cu^{2+} , it is commonly assumed that CuO possesses a mixture of ionic and covalent interaction. A monoclinic CuO crystal with $c2/c$ symmetry is shown in Figure 1. Cupric oxide's lattice parameters are 4.6837 \AA , $b = 3.4226 \text{ \AA}$, $c = 5.1288 \text{ \AA}$, $\beta = 99.54^\circ$ and $\alpha = \gamma = 90^\circ$.

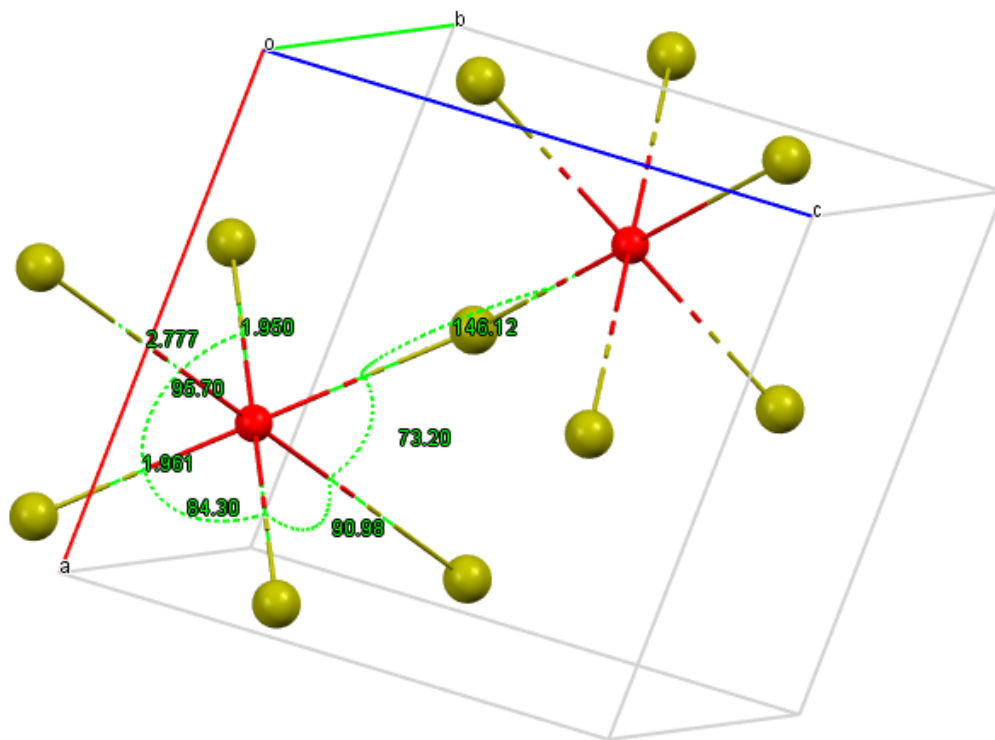


Figure 1 CuO Unit Cell (Red ball "Cu," Yellow ball "O ")

1.1.2 - Cu_2O -

$\text{Pn}3\text{m}$ or $\text{Oh}410$ is the space group. It has six atoms in its unit cell, with four copper atoms arranged in a face-centered cubic lattice (turquoise balls) and two oxygen atoms arranged in tetrahedral sites to form a body-centered cubic sublattice, as shown in fig3. As a result, oxygen atoms (Red Ball) are fourfold coordinated as nearest neighbors with copper atoms (Blue Ball), while copper atoms are linearly coordinated with two oxygen atoms as nearest neighbors.

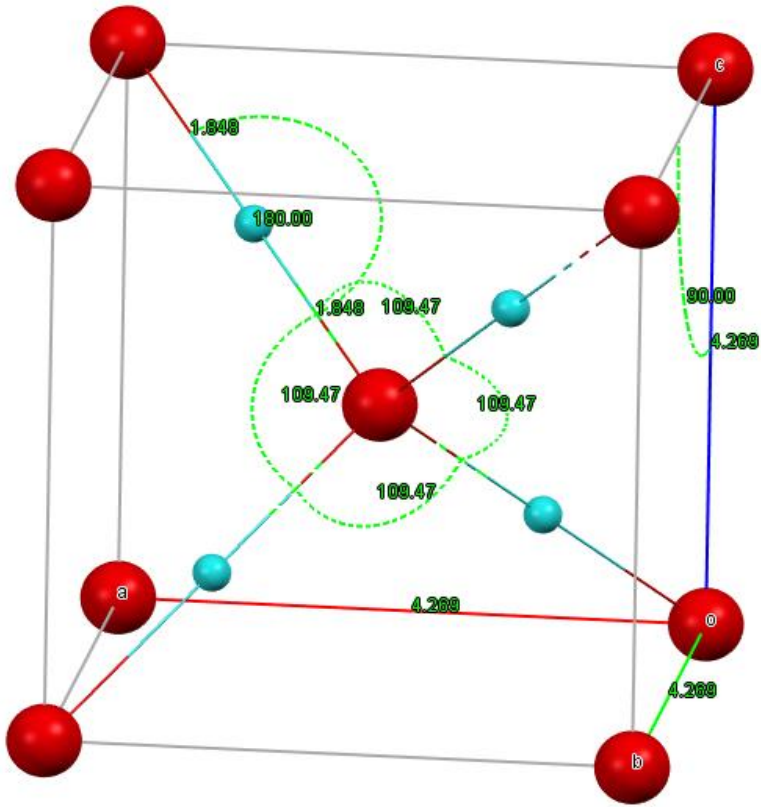


Figure 2 Cu_2O Unit Cell

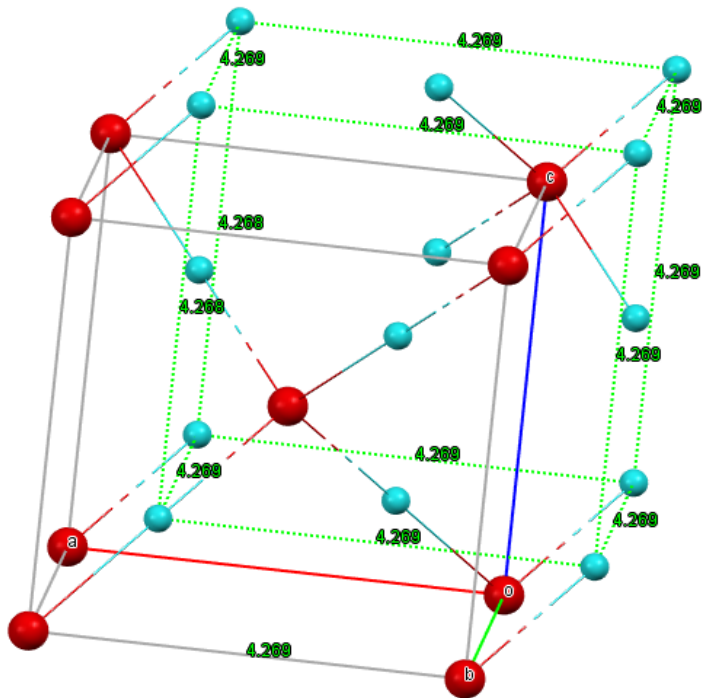


Figure 3 Cu_2O FCC and BCC unit cells

1.2 Fundamental Properties and Application

CuO first caught chemists' attention as a suitable catalyst for organic reactions. CuO is still a hot subject for physicists and materials science engineers due to newly discovered applications such as high-T_c superconductor, gas sensor, solar cell, emitter, and electronic materials.

1.2.1-Sensing Applications-

CuO is a suitable material for semiconductor resistive gas sensing applications due to its surface conductivity. Many different compounds, such as CO, hydrogen cyanide, and glucose, are detected using CuO nanomaterial¹¹.

1.2.2 -CuO could also be a good candidate for solar energy conversion-

CuO has been widely used in photovoltaic applications. CuO thin films are potential materials for solar dye-sensitized cells and light-emitting diodes. In the search for a clean and economical energy source, CuO is receiving growing interest from the scientific community. CuO can be used as an absorber in solar cells for direct solar energy transformation into electricity. An enhancement in the performance of OLEDs is reported by mixing CuO and Cu₂O in specific ratios¹². However, the mixed stoichiometry of CuO and Cu₂O has many defects (V_O, V_{Cu})¹³. These defects act as an additional energy level within the bandgap of mixed CuO/Cu₂O, increasing the hole injection efficiency. Also, good quality nanostructures with a high surface area may increase CuO-based solar cell efficiency.

1.2.3 -Photocatalytic activity

Water pollution is a major problem today because many organic compounds in wastewater are toxic and cannot be decomposed by themselves. Semiconductor catalysts can be effectively utilized under solar UV or visible light to decompose these organic compounds without much complication¹⁴. CuO is one promising material for the degradation of organic contamination and water splitting because of its narrow bandgap¹⁵. CuO generates electron-hole pairs under visible light illumination. This process further creates hydroxyl radicals (*HO) from water, which can mineralize organic components. In the water-splitting process using CuO, holes which are the majority carriers oxidize water to O₂, and the photogenerated minority electron charge carriers reduce water to H₂¹⁶. The addition of a few percentages of H₂O₂ in CuO enhances the photocatalytic properties of CuO nanomaterials. The shape and size of CuO greatly influence the photocatalyst properties of CuO.

CuO nanowires have attracted considerable attention for photocatalytic degradation of organic dyes.

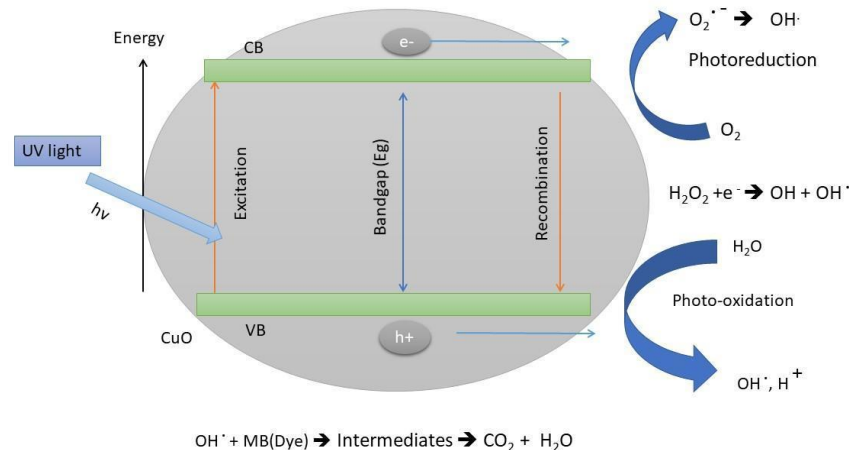


Figure 4 Electron Hole pair generation under UV illumination by nanoparticle

1.3 - Literature Survey-

The fast recombination of photogenerated electron-hole pairs limits the catalytic application of pure CuO due to its decreased catalytic activity. Doping with noble metals or rare earth metals is one approach to prevent electron-hole pairs from recombination. Some of the methods for modifying CuO that have been reported include adding a low percentage of metal, doping, impregnation of CuO with a metal salt, adding a low percentage of non-metal, CuO supported on porous materials, co-doping with two metals or metal and non-metal, loading metal halides and coupling two metal oxides. The effects of indium on the optical band gap and conduction mechanism of dip coated CuO films have been documented¹⁷. CuO films doped with 15% Ru had a higher specific capacitance and a broader potential window than CuO films that were not doped¹⁸. Due to the extended lifetime of the photogenerated charge carriers²⁰, the effects of Mn doping on CuO films' electrical and magnetic properties¹⁹ have been documented. Doping with 5% Li enhances the conductivity of CuO films by two orders of magnitude²⁰. When doped with 10% Fe, the Eg values of spray formed CuO films increased from 1.66 to 1.96 eV, and the magnetization at 300 K showed hysteresis behavior with large values²¹. Due to the extended lifetime of the photogenerated charge carriers, the effects of Mn doping on CuO films' electrical and magnetic properties Aside from alkali and transition metals, producing rare-earth-doped nanoparticles, with their optical characteristics and minimal cytotoxicity, has been one of the most active study fields in the last decade. CuO nanoparticles have potential use in solar energy transfer, sensors, storage devices, and superconductors. According to Aparna Y et al., in chemical processes, CuO nanoparticles work well as catalysts. Sahay R, et al. fabricated highly crystalline CuO nanofibers with possible energy applications analyzed the effect of the dwelling time of the annealing cycle for the formation of the crystallite CuO nanofibers and observed with an increase in the dwelling time, the crystallite size of CuO nanofibers decreased and results in the improved orientation of the CuO nanofibers. The highly

ordered morphology obtained at 12 h was employed for the photo-catalytic study. A 25% increase in the current density was observed with the application of CuO as a blocking layer. Wongpisutpaisana N et al. proposed that a sonochemical synthesis generates well-defined CuO nanoparticles with ultrasound help, with a reaction duration of up to 30 minutes and calcination at 600-700 °C. It was also discovered that the crystallization and particle size of the substance was highly influenced by the reaction time and calcination temperature.

The research work reported in the present thesis has been accomplished systematically in the following manner-

- ❖ Synthesis of CuO/Cu₂O composite
- ❖ Structural analysis of composite CuO/Cu₂O
- ❖ Structural analysis of CuO and its doping with Fe, Ti
- ❖ Effect of Doping on Strain, lattice parameters and other structural properties
- ❖ Optical properties of Composite CuO/Cu₂O and Pure phase CuO and its effect by doping of Fe, Ti
- ❖ UV sensing application of Transition metal doped CuO samples
- ❖ Photocatalysis on CuO/Cu₂O Composite

Chapter 2

2 - Experimental Details

In this chapter, we shall briefly discuss the process of sample preparation and the different characterization techniques used in studying the prepared samples. All the samples in this study have been prepared using the sol-gel method. Characterization techniques used in this study include-

- ❖ X-ray diffraction (XRD) to study the structural properties
- ❖ UV-Vis's spectroscopy to study the optical bandgap properties
- ❖ The electrical properties: I-V measurements are made using a Keithley source meter 2450
- ❖ UV & Visible Light Sensing was done using a homemade setup.

2.1 - Synthesis Process

The synthesis process used for synthesizing all the materials used in this study was done using the sol-gel method. Sol-gel chemistry is a method of creating inorganic polymers or ceramics from a solution by converting liquid precursors to sol and then to a network structure known as a 'gel.' Solid ion particles suspended in a colloidal solution ($1 \text{ nm}^{-1} \mu\text{m}$) in a solvent is called a sol. A gel is the formation of a semi-rigid mass when the solvent starts to evaporate from the sol and the particles/ions left behind; Metal oxides are formed by joining the metals with oxo or hydroxy chains. This results in the formation of metal-oxo or metal-hydroxo polymers in the solution. Next, the gel is dried to remove the liquid phase from it and form a porous powder. After this, calcination and annealing may carry out²². Generally, water-soluble precursors such as metal nitrates and metal acetates are used for material synthesis.

The following are steps involved in the sol-gel process:

Hydrolysis → Condensation → Gelation → Aging → Drying → Calcination

The stages of the Sol-Gel process

Hydrolysis of precursor (sol formation)- $\text{M-OR} + \text{H-OH} = \text{M-OH} + \text{R-OH}$

Polycondensation (gelation)-



2.1.1 - Chelation-

Controlling the solgel transformation, which includes controlling the alkoxide hydrolysis rate, is necessary to achieve uniformity and microstructure in the final product. Alkoxides must be adjusted to control the hydrolysis process by replacing a portion of the alkoxy groups with ligands(h-L) that have better hydrolysis stability. The procedure entails generating a chelate between mixed cations (salts dissolved in water) and a hydroxycarboxylic acid (citric acid is preferred). The cations are first chelated, and then the chelates are crosslinked with polyalcohol to form a gel through esterification. This offers the specific advantage of allowing metals without stable hydroxo species to be used. Pechini began by using citric acid (CA). This is frequently substituted by EDTA (ethylenediamine tetraacetate), which benefits from chelating most metals and is easily crosslinked to create a gel due to its four carboxylate groups. It is also conceivable to use polyvinyl alcohols that provide for a three-dimensional network during gel formation²³.

2.1.2 - Aging and Drying-

Polycondensation continues with the solution immersed during the aging phase, and the gel network will reprecipitate. The wet gel is heated to around 100°C throughout the drying process to allow for the desorption of physically bonded water and alcohol. The simple evaporation of a wet gel into a dry gel causes distortion of its fundamental porous backbone, which frequently results in the creation of "cracks." Chemical mechanisms, such as condensation reaction, and physical factors, such as capillary pressure, are driving forces for shrinking. The lattice would be uniformly squeezed if the pressure in the liquid was uniform, and there would be no tendency to fracture. The gel's limited permeability, on the other hand, results in a pressure gradient. The creation of cracks is caused by a variation in contraction speed between the inner and outside of the gel. The gel's warping and breaking can be mitigated by aging it. The chemical events that cause gelation are proven to continue long after the wet gel is formed, resulting in changes in the gel's physicochemical properties. The production of new crosslinks causes shrinkage (syneresis), which raises the gel's modulus and viscosity, reducing further shrinkage during drying. During this stage, the water and other liquids caught within the pores of the gel structure are removed. The drying process is carried out at a temperature of around 400° F²⁴.

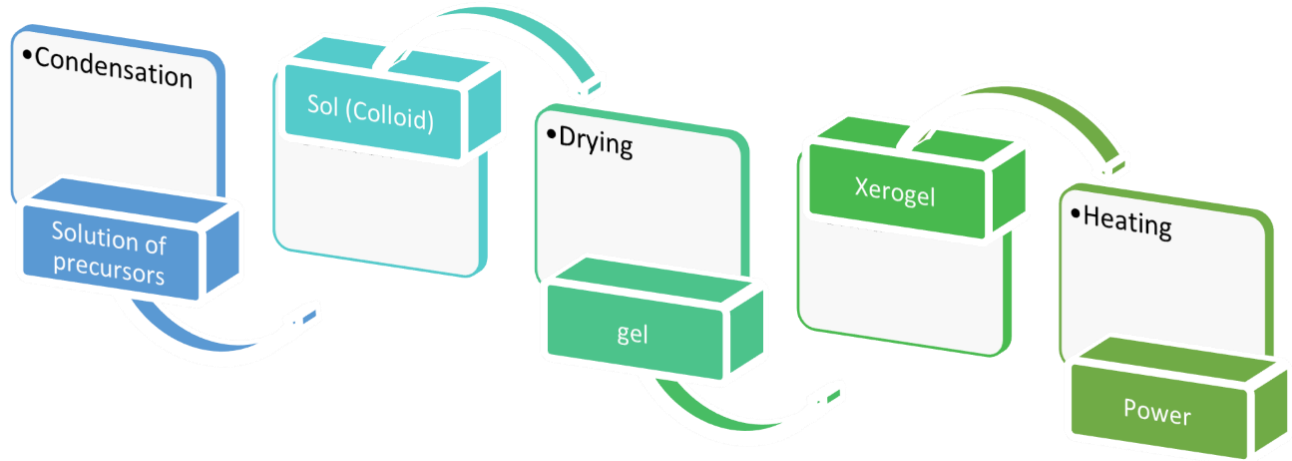


Figure 5 Sol-Gel method

2.2.1 -Synthesis of CuO/Cu₂O Composite-

1M solution of Cu (Ac) was prepared in DI water. NH₄OH (ammonium hydroxide) is used as an alkaline base medium. A pH~10 of the medium is maintained. Solution of Cu (Ac) and NH₄OH was stirred for 1hr and heated continuously at 60°C. Finally, a powder is formed after prolonged heating ~3hr in the ambient atmosphere. The obtained powder is gently grinded to get a smooth homogeneous powder. The obtained powder is heated at 250 °C (hereafter called S250) and 500 °C (hereafter called S500) in a closed tube furnace.

2.2.2 - Synthesis of Fe -Doped CuO-

Cu_{1-x}Fe_xO (x=0, 0.0156, 0.0234, 0.0312), hereafter named as Fe-0, Fe-1, Fe-2, and Fe-3, have been synthesized by using the sol-gel process followed by the solid-state reaction method.

The samples were made using Copper (II) oxide (99.97 percent, Alfa Aesar) Iron Nitrate nonahydrate as a precursor. CuO was dissolved in dilute HNO₃ to make the Cu precursor solution. Fe³⁺ precursor is added after creating a homogeneous solution in Double Ionized water through constant stirring, and the two are violently agitated together. Citric acid and glycerol were utilized as gelling agents. The solution was then heated for four hours to form a gel. A black powder was eventually detected. After that, samples were denitrogenated and decarbonized at 450°C to eliminate nitrates and carbon components. After that, the annealing of samples was done at 600°C. The final nano-powder was obtained and grinded smoothly, and then characterization explained in the next section was done.

2.2.3 - Synthesis of Ti Doped CuO-

$\text{Cu}_{1-x}\text{Ti}_x\text{O}$ ($x=0, 0.0156, 0.0234, 0.0312$), hereafter named as: Ti-0, TI-1, Ti-2, Ti-3. For the synthesis of titanium doped copper oxide, we used the aqueous sol-gel method. Copper oxide, nitric acid, ethylene glycol, citric acid, TALH [Titanium (IV)bis (ammonium lactate) dihydroxide], and double-distilled water were needed to produce the nanostructure. At varied doping doses ($x=, 0.0156, 0.1234, 0.0312$), we synthesized pure and Ti-doped CuO. Precursors for doped phases are made by dissolving copper oxide and TALH in appropriate volumes of double-distilled water. After that, the solution is agitated, and nitric acid is added dropwise while swirling continuously. After 2 hours, a 1:2 ratio of citric acid and ethylene glycol is added to the solution. Following that, the gel is formed. The final product is obtained by heating at high temperatures. $\text{Cu}_{1-x}\text{Ti}_x\text{O}$ nanocrystals are formed by annealing the material at 450°C and 600°C .

2.3 - Experimental Techniques Used-

Several experimental approaches, such as XRD (for structure), Raman (for vibrational), and UV-Visible spectroscopy, Light Sensing, were used on samples.

2.3.1 - X-Ray Diffraction

W.H. Bragg and W.L. Bragg discovered in 1913 that substances with crystalline macroscopic forms diffract X-rays when they fall on them. It is because the distance between atoms in crystalline solids is equivalent to the wavelength of an X-ray, which is a requirement for diffraction to occur in crystals.

The primary electron loses measurable energy(E) when a high-energy electron interacts inelastically with an atom. Phonon scattering, Plasmon scattering, characteristic X-ray, bremsstrahlung X-ray, auger electron generation, and other phenomena will result from this interaction.

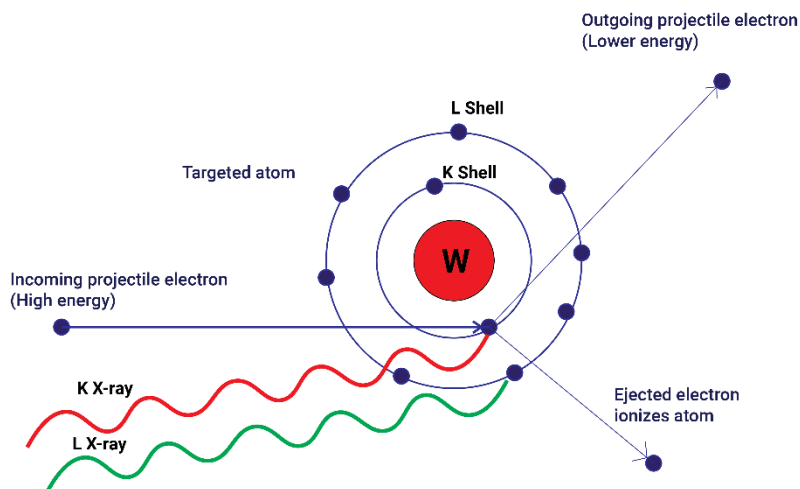


Figure 6 Characteristic X-ray generation

2.2.1.1 - Principle

Crystalline solids behave as a diffraction grating for X-rays; Diffraction peaks result from constructive interference between diffracted monochromatic X-rays. The more photon energy the originating electron has, the more electrons there are, the higher the X-ray beam's intensity. Bremsstrahlung (Braking radiation) and Characteristic X-ray are the two types of X-rays in the spectrum (radiation involving the transition of inner shell electrons). When electromagnetic radiation with a wavelength λ equal to atomic spacing 'd' strikes a crystalline sample, it is scattered by the atoms in the system and undergoes constructive interference, as shown in the picture.

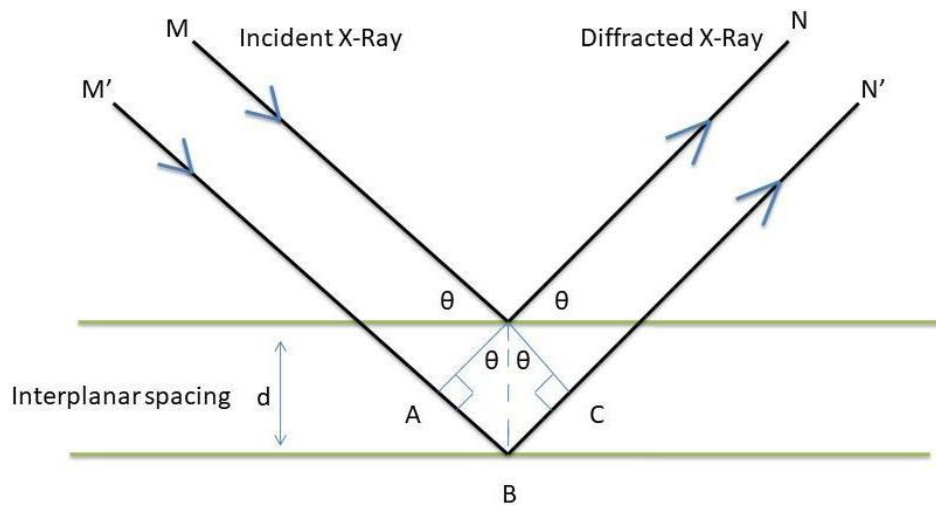


Figure 7 Bragg's diffraction

the overall path difference between the two beams.

$$= AB + BC$$

$$= d\sin\theta + d\sin\theta = 2d\sin\theta$$

If this path difference is equal to an integral value 'n' of the wavelength of incident X-rays, i.e.,

$2d\sin\theta = n\lambda$, the two independent waves will arrive at a place with the same phase and suffer constructive interference. This is Bragg's diffraction law.

A powder X-ray diffractometer consists of 3 parts:

- a) An X-ray source (usually Cu-K α radiation)
- b) A sample stage
- c) A detector

Sources of X-ray generation are radioisotopes and secondary fluorescence; the most common source of X-rays is copper (Cu-K α of $\lambda=1.5418 \text{ \AA}$) and molybdenum. These X-rays are directed onto the sample mounted on the sample stage at some angle θ . In contrast, the detector opposite to the source detects the intensity of the diffracted X-ray received at an angle 2θ away from the source path. As the detector is rotated, the intensity of the reflected X-rays is recorded. When the crystal's geometry satisfies the Bragg's condition, then a diffraction peak occurs, which is recorded.

2.3.1.2 System specifications:

Model: Bruker D2 Phaser x-ray diffractometer

Max Power: 3 kW

X-ray target: Cu anode (K $\alpha = 1.5406 \text{ \AA}$)

Operating voltage: 30 kV

Optics: Bragg Brentano, Parallel beam

2.3.2 - Field emission scanning electron spectroscopy

The surface morphology of the material is imaged using Field Emission Scanning Electron Microscopy (FESEM). An electron beam, like the light in an optical microscope, is employed as a source for imaging. It produces high-quality, low-voltage pictures in samples with minimal electrical charging. An electric field triggers electron emissions in the field emission process. This allows for smaller probing beams to be generated at both low and high electron energies. A field emission source can provide high spatial resolution and reduce sample damage/charging. To picture things on the nanometer scale, better resolution in the range of a few nm is required, which necessitates the use of light with a wavelength of nm. The fine electron beam spot has a significant advantage over the visible light spot regarding spatial resolution. FESEM produces better, less distorted images with a spatial resolution of 1 nm, superior to optical microscopes and SEMs. Secondary electrons (SEs), backscattered electrons (BSEs), Auger electrons, X-rays, and other rays are produced when energetic electrons interact with materials. To create pictures, FESEM employs SEs and BSEs, and x-rays for elemental/composition analysis.

a - Secondary electrons (surface morphology): The surface of the materials is imaged using secondary electrons. These come from the sample's near-surface areas (less than 10 nm). The inelastic interactions between the primary electron beam and the sample are responsible for creating these electrons. Hence the analysis of the morphology of the sample's surface benefits from secondary electrons.

b - Backscattered electrons (composition contrast): Electrons are backscattered from a large area within the interaction volume. The elastic collisions of electrons and atoms that result in a shift in the electrons' trajectory are

the source of these electrons. The so-called "billiard-ball" paradigm, in which smaller particles (electrons) collide with larger particles (atoms), can explain this behavior. The number of backscattered electrons that reach the detector is precisely proportional to their 'Z' number, which aids in phase discrimination. In addition, it provides imaging that conveys information about the composition of the sample.

c- Energy-dispersive X-ray spectroscopy: EDS, EDX, and EDXS are all acronyms for energy-dispersive X-ray spectroscopy, a technique for elemental analysis. It can determine the relative amount of each element and map the element's distribution. FESEM includes EDX as a component.

2.3.2.1 - X-ray generation is a two-step process in FESEM.

First step: An electron beam strikes on the sample and transfers its energy to the sample's atoms. As a result, the electrons could jump to a higher energy shell or be knocked off from the atom. After this transition, holes are created.

Second step: Higher energy shell electrons recombine with lower energy shell holes—the energy difference of these two shells is released in the form of x-rays. The generated X-ray is related to the atomic number and the unique property of each element. The energy of these transitions is used to identify the elements.

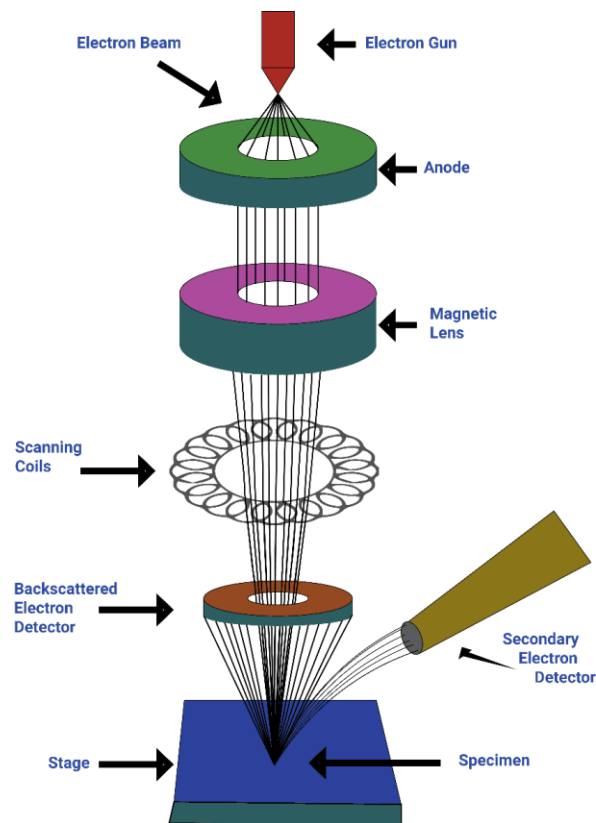


Figure 8 Schematic diagram of Field Emission Scanning Electron Microscope

2.3.3 - UV-Vis Absorption Spectroscopy-

Several processes happen when electromagnetic radiation interacts with material, including reflection, absorption, transmission, and scattering. These processes take place all around us daily; but, if we investigate them, they can reveal information about the sample. For example, when a red ball is illuminated by white light, it appears red because it absorbs all other wavelengths of the input radiation, leaving only a red hue. Similarly, all light on glasses is transmitted because incident radiation does not have enough energy to excite the glass's SiO₂ electrons. Therefore, they do not absorb any radiation and allow the light to pass through. There are primarily two types of Reflectance: Specular Reflectance and Diffused Reflectance

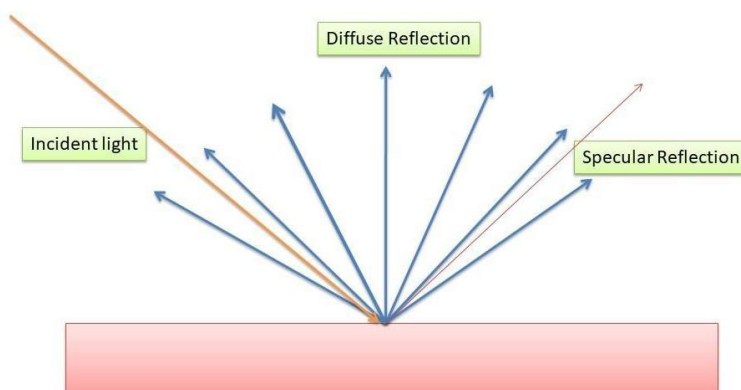


Figure 9 Schematic of Specular and Diffuse reflection

Specular: It is also called "mirror-like" reflection; when radiation is incident on the perfectly ordered interface and they have an imperfection in order less than the wavelength of the incident light, the reflected light angle will be the same as incident light angle and reflected light would go in a straight line, and most of the light has been reflected in this case such as Polished metal surfaces, glass, liquid surfaces.

Diffused: When the order of imperfection is larger than the incident radiation, the radiation gets reflected in many directions, and there is more absorption in this case Diffused reflection is used in UV visible and Near Infrared (NIR) spectroscopy

Principle

When radiation of intensity is incident on a surface of some width, and it absorbs some part of intensity and transmits remaining, the relation between the incident and transmitted radiation is given by Beer-Lambert law:

$$I = I_0 e^{-\alpha t}$$

here α is the coefficient of absorption, shown as (for $t=1$)

$$\alpha = -\ln\left(\frac{I}{I_0}\right)$$

Absorption light intensity is the difference between incident and transmitted light intensity. The ratio of transmitted light intensity to the incident light intensity is:

$$T = \frac{I}{I_0}$$

Here T, I₀, I are called Transmittance of the material, incident intensity, transmitted intensity, and sample width, respectively at a particular wavelength. T=1 for a purely transmitted sample. Similarly, for diffuse reflective samples, the ratio of reflected light intensity to incident light intensity is.

$$R_{\infty} = \frac{J}{J_0}$$

Here R_∞, J is called absolute remittance and reflected light intensity. Subscript ∞ refers to the fact that in absolute remittance, we have considered the sample infinitely thick. Hence, all that there is no transmittance, and incident light never penetrates the sample holder. since this, not the case always, the quantity we measure is called relative remittance, which is $R'_{\infty} = \frac{R_{\infty \text{ sample}}}{R_{\infty \text{ standard}}}$

For and reflected sample R_{∞standard} = 1 and R_{∞'} = R_{∞sample}. In the case of Transmittance, it is always convenient to represent data in the absorption unit as absorption is linearly proportional to absorbing material according to Beer's law. Beer's law gives the relation between the absorption coefficient and the Transmittance of the material

$$\alpha = \ln\left(\frac{1}{T_0}\right)$$

Diffuse reflectance spectroscopy (DRS) is used to obtain the bandgap of powder samples as they are scattered in a perfectly diffused manner. It follows on Kubeka-Munk theory which gave a similar function for diffusive

$$\text{Reflectance as } F(R_{\infty}) = \frac{(1 - R_{\infty})^2}{2R_{\infty}} = \frac{K}{S} = \frac{K2.303C\varepsilon}{S}$$

Here F(R_∞), R_∞, K, S, C, ε, S are Kubelka-Munk function, percentage of Reflectance of material, absorption Coefficient, S is twice the scattering Coefficient of material, C is analyte concentration, and ε is absorptivity, respectively. Here K is twice the Beer's Law absorption coefficient.

Kubelka-Munk function is proportional to the absorption coefficient now the above equation can be written as:

$$F(R_{\infty}) \propto \alpha \propto \frac{(h\nu - E_g)^{\frac{1}{n}}}{h\nu} \Rightarrow (ah\nu)^n = A(h\nu - E_g)$$

Here h, ν, E_g, A, and n are plank constant, frequency of incident radiation, the bandgap of material, the proportionality constant, and the quantity that lets about the transition's nature. n=2 for direct allowed changes.

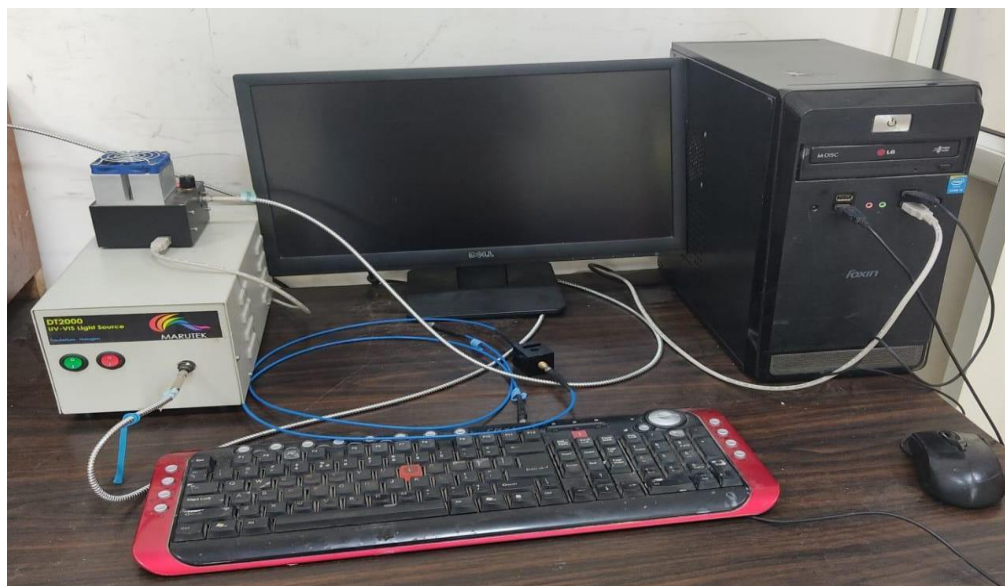
Tauc et al. proposed to estimate the bandgap of samples from absorption data using the Bloch theorem. Davis and Mott enhanced it for all material and concluded that a plot of $(\alpha hv)^n$ vs. hv could find a linear region that will be used to find the Bandgap E_g . The graph where we plot $(\alpha hv)^n$ vs. hv is called the Tauc Plot. This graph will be of state line such as $y = mx + c$. After linearly fitting it for a straight line, we will get the value of slope and intercept; the ratio of intercept to the slope will give us the bandgap of the system. Reflectance data can also be used to calculate the Urbach energy E_U of the sample, which essentially tells about the degree of structural disordering or poor crystallinity. E_U can be calculated from the slope of a logarithmic plot of $\ln[\alpha]$ and hv as

$$\ln \ln [\alpha] = \ln \ln [\alpha_0] + \left[\frac{hv}{E_U} \right]$$

Here α , α_0 , h , ν , and E_U are absorption coefficient, absorption constant, plank constant, frequency of the incident light, and Urbach energy, respectively

2.3.3.1 Instrumentation-

The instrumentation key components are the same as any other spectrometer, such as source, monochromator, beam splitter, sample holder, detector, signal processor, and readout. Here a Tungsten-halogen or Deuterium lamp is used as a source to create UV light in the range of 200nm to 1100 nm; radiation is passed through a monochromator to select a single wavelength then this radiation is passed through a beam splitter which divides it into two-part one part is sent directly to the detector and another part to the sample. The sample now absorbs some parts and reflects the rest of the part, which is currently sent to another detector. The detector used is photodiode or CCD detectors. Now signal processors calculate reflectivity and save data of reflectivity for every hv value. A schematic diagram of the instrument is given in the figure.



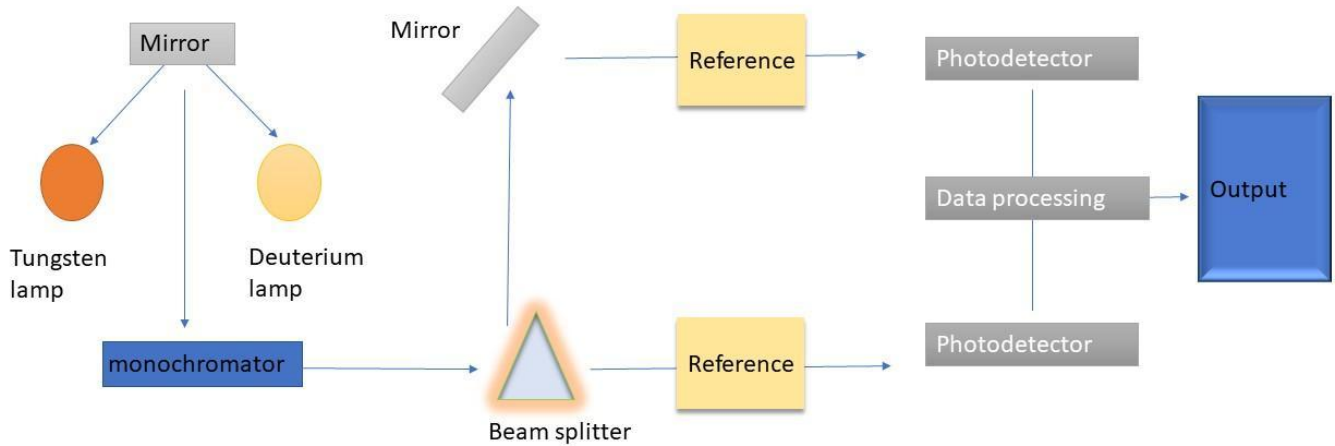


Figure 10 UV-Vis setup and Schematic diagram of the UV-Vis spectrometer

2.3.4 - Set up for UV and Visible Light sensing:

The UV and visible light sensing apparatus were built in-house to investigate the response and sensitivity of prepared samples when exposed to different wavelengths of light.

Instrumentation: The setup includes:

- ❖ UV lamp that emits UV light with a wavelength of 290 nm.
- ❖ Red, Green, and Blue LEDs with wavelengths of 640 nm, 540 nm, and 450 nm.
- ❖ A dark chamber to contain the sample and the light source.
- ❖ Uno Arduino
- ❖ A computer (computer)

A relay linked to an Arduino UNO is used to link the UV lamp and LEDs to the power source. The Arduino may be configured to regulate the light source's ON and OFF states automatically. The sample is maintained in a dark box with only a small amount of light falling on it. Electrodes are joined to the Keithley to calculate the response.

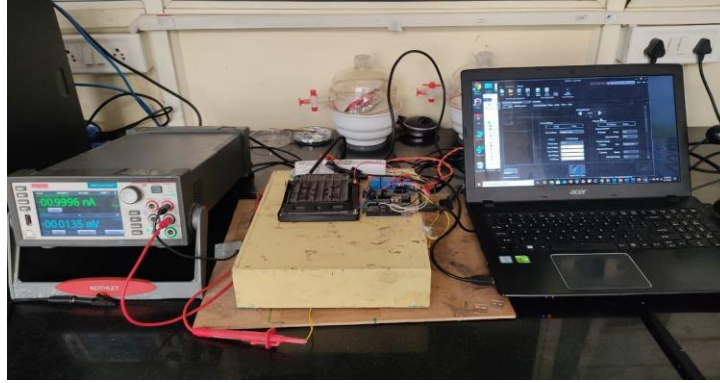


Figure 11 a schematic diagram for the UV to Visible light sensing setup along with photographs of the different wavelengths of light

2.4 - Rietveld Refinement-

Rietveld refinement was performed to quantitatively analyze various structural parameters from the powder x-ray diffraction data. Developed by Hugo Rietveld, this technique creates a hypothetical structural model representative of the crystal, considering the dimensional parameters of the instrument. A simulation is performed with this model's parameters, and a diffraction pattern is generated, which is matched with the observed/experimental XRD data pattern. The simulation involves all the parameters that may affect diffraction peaks. The minimum least square fit is obtained for a specific set of parameters accepted as the refined structural parameters of the sample. An initial crystal structure model of a similar structure or a derivative structure is accepted as a starting point for refinement. A regression algorithm refines parameters to reduce the difference between the simulated (calculated) and experimental patterns. Different parameters are selected, such as background, error-correcting parameters, lattice parameters, peak profile parameters, etc. We have performed Rietveld refinement of the high-resolution powder x-ray diffraction pattern data in the present samples studied. A good fit of experimental data after refinement is estimated by assessing the values of R-factors. These parameters provide the difference between calculated and observed XRD data, and the difference can be evaluated and expressed as a series of numerical coefficients. The

weight profile R-factor is denoted as R_{wp} and is given by the formula: - $R_{wp} = \left[\frac{[\sum_i w_i (y_i(obs) - y_i(calc))^2]^{1/2}}{[\sum_i w_i (y_i(obs))^2]} \right]$

Where w_i is the weighting factor, $y_{i(obs)}$ is observed (experimental) intensity, and $y_{i(calc)}$ the intensity from the calculated model. The $y_{i(obs)}$ and $y_{i(calc)}$ will include the background refinement. For an ideal fit, the final R_{wp} should

tend to the statically expected R-value, R_{exp} , is described by the formula: - $R_{exp} = \left[\frac{(N-P)}{\sum_i w_i (y_i(obs))^2} \right]^{1/2}$

Where N is the number of observations, and P is the number of parameters. Thus, R_{exp} reveals the quality of the experimental data, and R_{wp} gives an overall view of the quality of Rietveld refinement. To estimate the excellent

fit, describe the ratio of R_{wp} and R_{exp} . This is a good indicator and given by the formula: $\chi^2 = \left(\frac{R_{wp}}{R_{exp}} \right)^2$

Information from Rietveld refinement:

- Crystal structure and phase purity.
- Lattice parameters of the unit cell.
- Atomic positions, fractional occupancy, and thermal parameters.
- Lattice strain and crystallite size.
- Relative phase fraction for mixed phases.

Description of crystal structure

- Space group.
- Unit cell parameters: lattice parameters (a, b, c) and angles (α , β , γ).
- Atomic positions.
- Atomic site occupancies.
- Atomic thermal parameters (Debye-Waller factor).

The parameters used for the simulation of the powder X-ray diffraction pattern.

	Instrumental Factors	Sample Based Factors
Peak Position	The wavelength, Zero-point error, Sample height	Unit cell dimension
Peak Shape	Diffractometer geometry, slit size, Type of detector, an X-Ray source	Size of crystallites, Strain, Defects
Intensity	Amount of sample, Lorentz- polarization, and Other diffractometer factors	Atomic Coordinates, Temperature factor
Background	Air scatter, Detector Noise, Sample Holder	Fluorescence, Disorder

The background of the XRD data was determined for Rietveld refinement in the current investigation for all samples by linear interpolation between the selected background spots of refinable heights. The pseudo-Voigt axial divergence asymmetry function was utilized to represent the Bragg peaks for all the compositions. After that, the scale, lattice, half-width, locations, and isotropic thermal parameters were refined. After numerous rounds of refinement, acceptable R-factors were found.

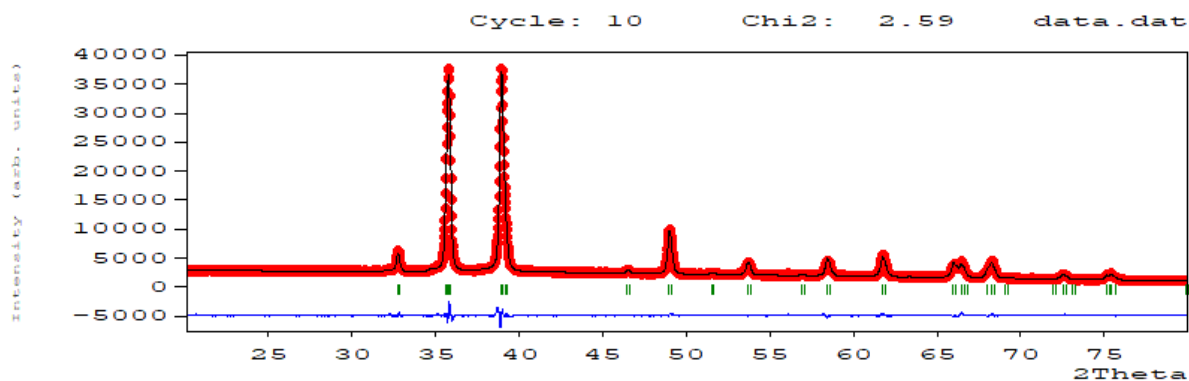


Figure 12 Rietveld Refined Pure CuO

Chapter 3

3.1 - Structural properties-

Phase calculation was done after the XRD was obtained from the Bruker D2 Phaser diffractometer. The structural analysis of all the samples was performed by doing the Rietveld refinement of the XRD data using GSAS-II software. The lattice parameters, bond lengths, and bond angles were obtained from the refined crystallographic information file (cif). Eva software was used to compute crystallite size and lattice strain, followed by the Tiny Tool XRD calculator, which uses the Scherer equation to calculate crystallite size, and the Williamson-Hall method for lattice strain calculations. The Scherer equation is given by: $B_c = 0.9 \lambda / (t \cdot \cos(\theta))$ while the Williamson-Hall equation is given by: $B_{total} = 0.9 \lambda / t + 4\epsilon \sin(\theta)$.

3.1.1 - Phase-detection of CuO/Cu₂O composite -

X-ray diffraction (XRD) uses a Bruker D2 Phaser diffractometer to investigate the structure of S250 and S500 samples²⁵. The S250 powders are mostly CuO phase with small contributions of the Cu₂O phase. On the other hand, the Cu₂O phase enhances in S500 samples. However, the CuO phase becomes weak. This is understood from the matched experimental data with the cif files of CuO and Cu₂O. Hence, with annealing, the Cu₂O phase becomes dominant, i.e., O leaves the lattice leading to a gradual structural change.

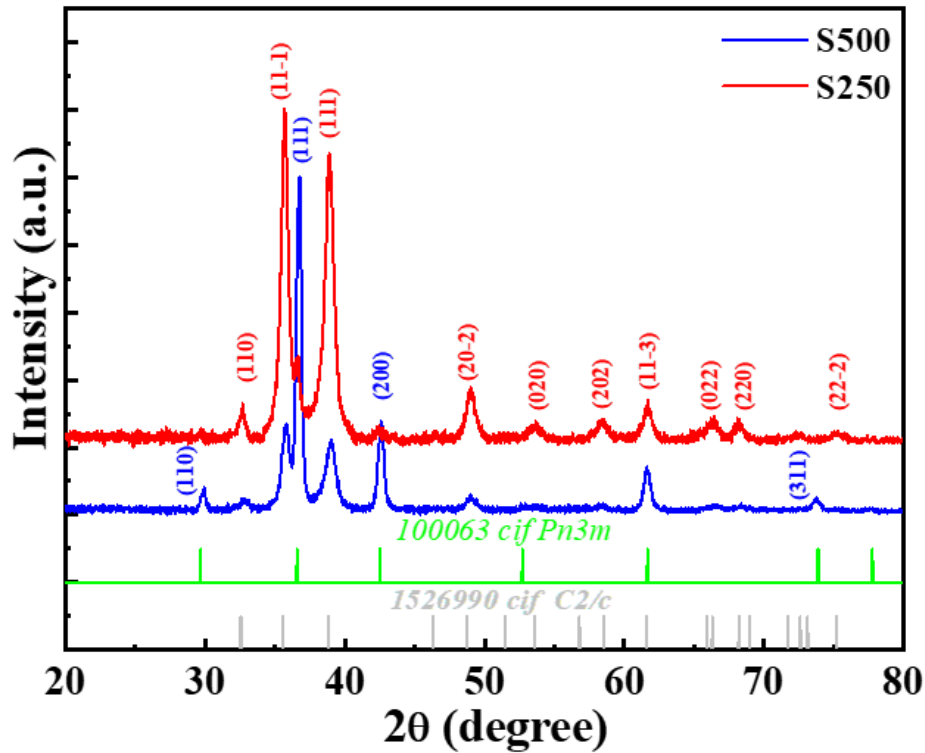
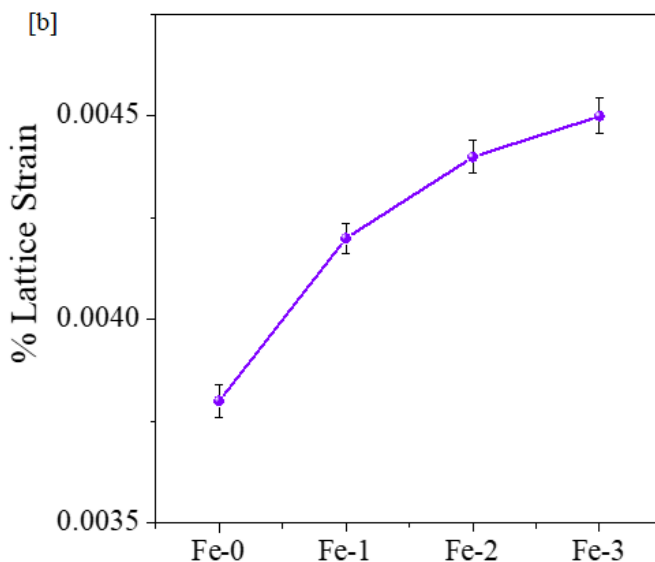
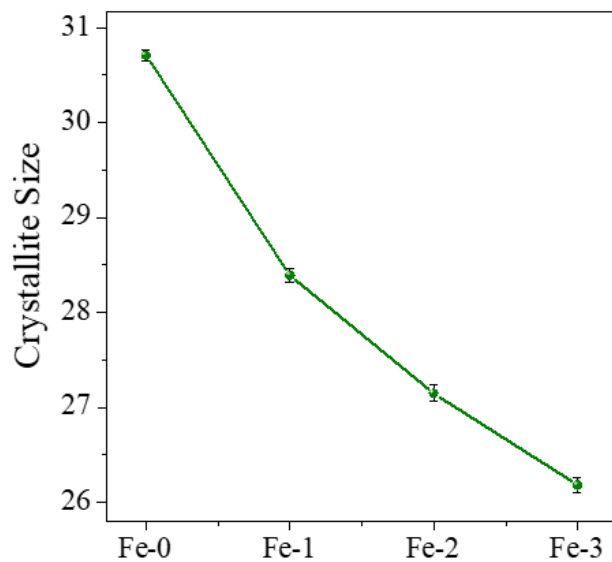
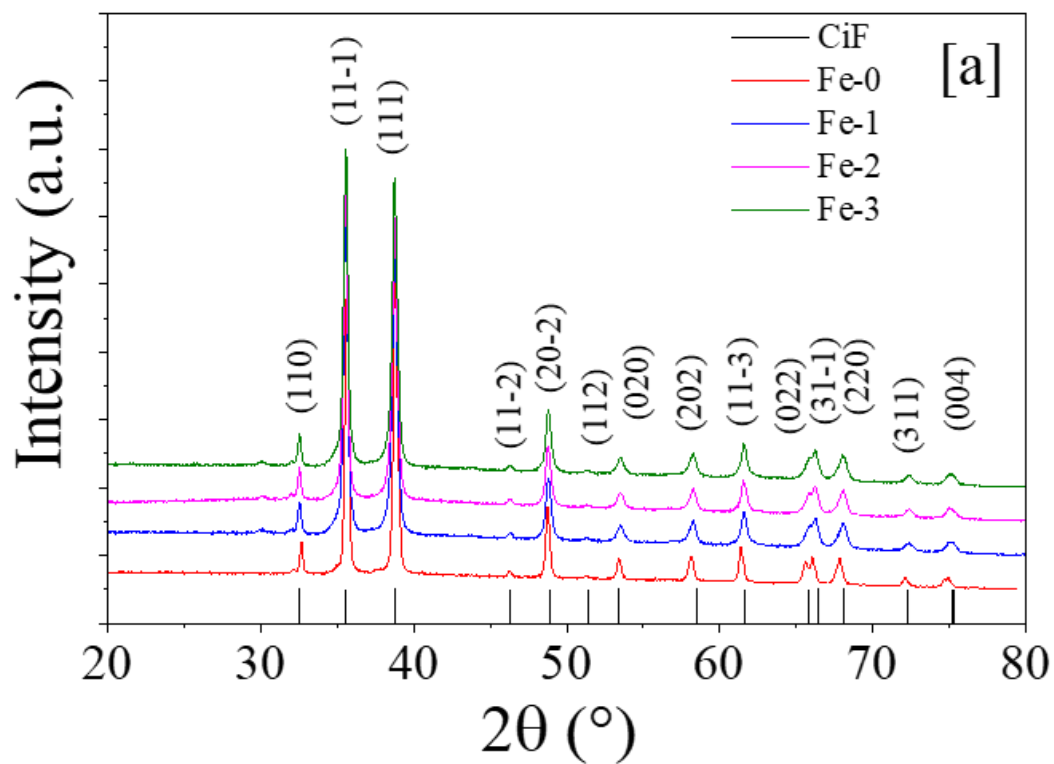


Figure 13: XRD pattern of S250, S500

3.1.2 - Effect on Fe Doping in CuO-

The XRD (X-ray diffraction) pattern of $\text{Cu}_{1-x}\text{Fe}_x\text{O}$ ($x=0, 0.0156, 0.0234$ and 0.0312 named as Fe-0, Fe-1, Fe-2 and Fe-3). The samples show a single-phase monoclinic structure with space group $c2/c$. Further, Rietveld analysis of $\text{Cu}_{1-x}\text{Fe}_x\text{O}$ was performed to investigate the structural parameters like lattice constants, bond-lengths, and bond angles were calculated from the *cif* files obtained after refinement. The lattice parameter ‘ $a(\text{\AA})$ ’ showed a significant increase for Fe-1 afterward varied insignificantly while lattice constant ‘ $b(\text{\AA})$ ’ is invariant but nominally decreased for Fe-3. However, the parameter ‘ $c(\text{\AA})$ ’ decreases continuously with Fe^{+3} doping. The contraction along the c -axis is logical because Fe^{3+} has higher charge and lesser ionic radii (0.63\AA) as compared to the host cation Cu^{2+} (0.71\AA). The introductory Fe^{3+} will invite extra oxygen to satisfy the stoichiometric charge balance. The extra charge of Fe^{+3} invites more oxygen into the lattice, thereby creating interstitial oxygen which should result in expansion of the lattice. However, the considerably smaller radius of Fe^{3+} compensates this expansion to some extent. Hence, the compression of lattice parameters can be explained and leads one to a possibility of compressive strain. With doping, the apical bond Cu-O_3 dropped and then remained constant. On the other hand, the bond angle $\text{O}_3\text{-Cu-O}_1$ increased, followed by a minimal change as Fe is increased. This hints at the possibility of an increase of lattice strain. The crystallite size decreases as the lattice strain increases. Literature suggests that, as bond length decreases, the lattice

strain increases²⁶. As the lattice parameters contract, a compressive strain is expected, which may affect the electronic properties and modify the bandgap.



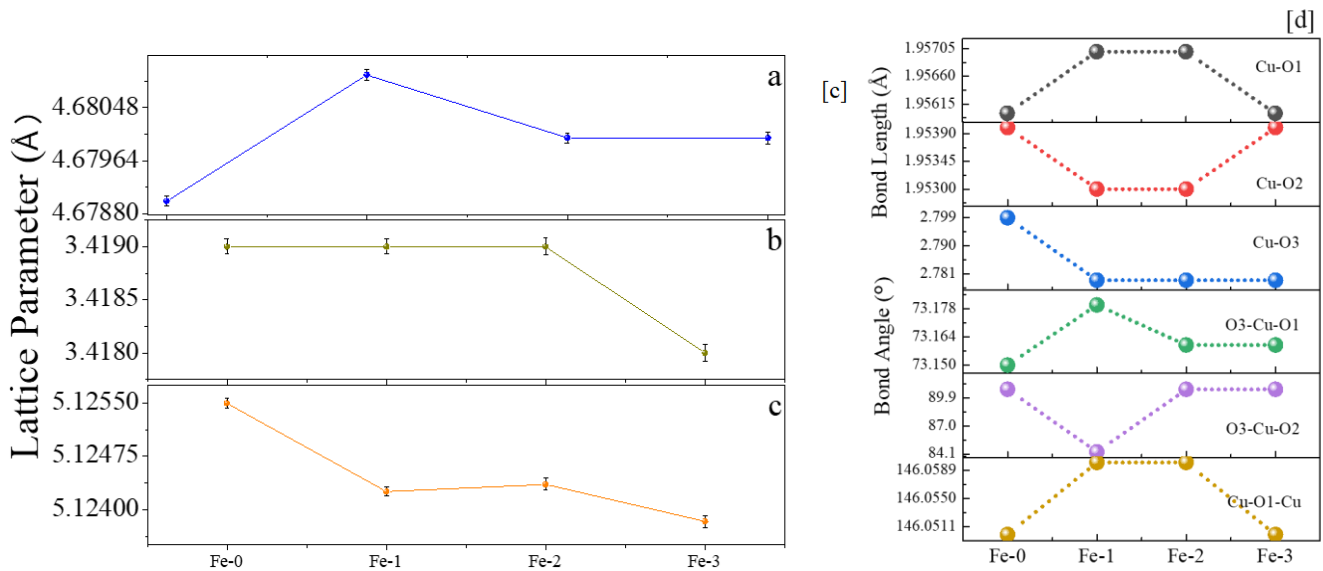


Figure 14 a- XRD Fe Doped CuO, b- Lattice Parameters, c- Crystallite size and Lattice Strain, d-bond length, bond angle

3.1.3 - Effect on Ti Doping in CuO-

The lattice parameters a, b, and c of the monoclinic lattice follows a similar trend of variation. The $Ti^{4+}(IV)$ (0.56 Å) is again smaller than the host $Cu^{2+}(IV)$ (0.71Å). Hence, the lattice parameters should decrease with Ti doping. However, the huge increase of the ionic charge of Ti will introduce larger proportions of oxygen into the lattice. Hence, an increase of oxygen interstitials $[O_i]$ is possible which can expand the lattice²⁷. All the lattice parameters a, b, and c show a significant lattice expansion with the introduction of Ti for Ti-0, Ti-1, Ti-2, and Ti-3. Such changes are precursors to changes in bond lengths, bond angles, and lattice strain and can affect electronic properties. As the lattice strain increases a reduction of the crystallite size is observed.

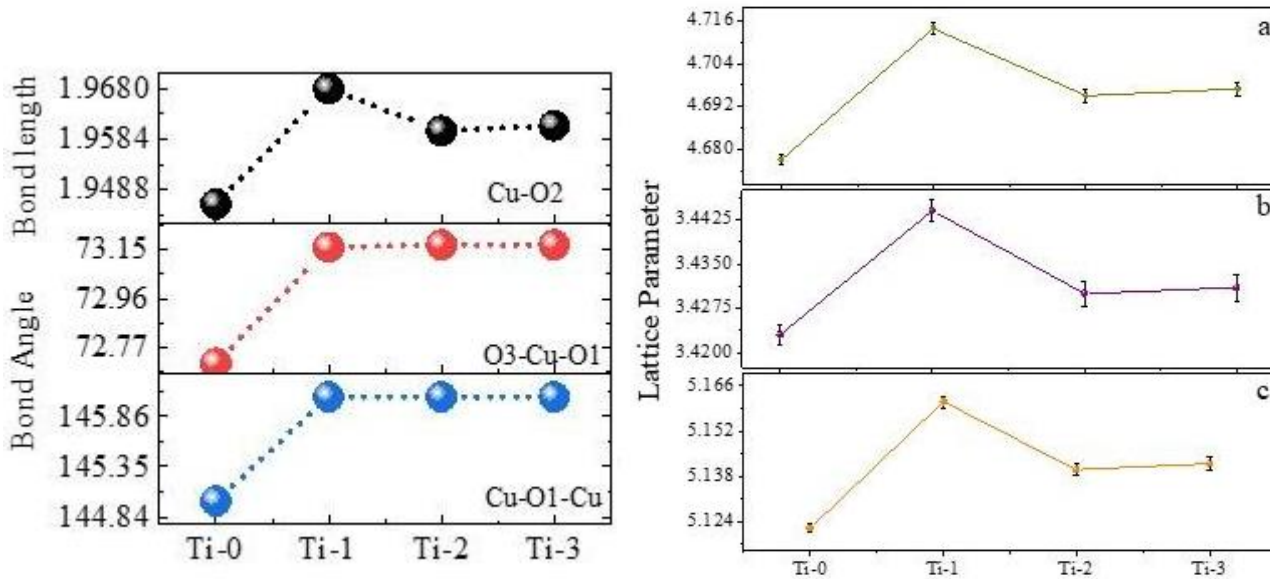
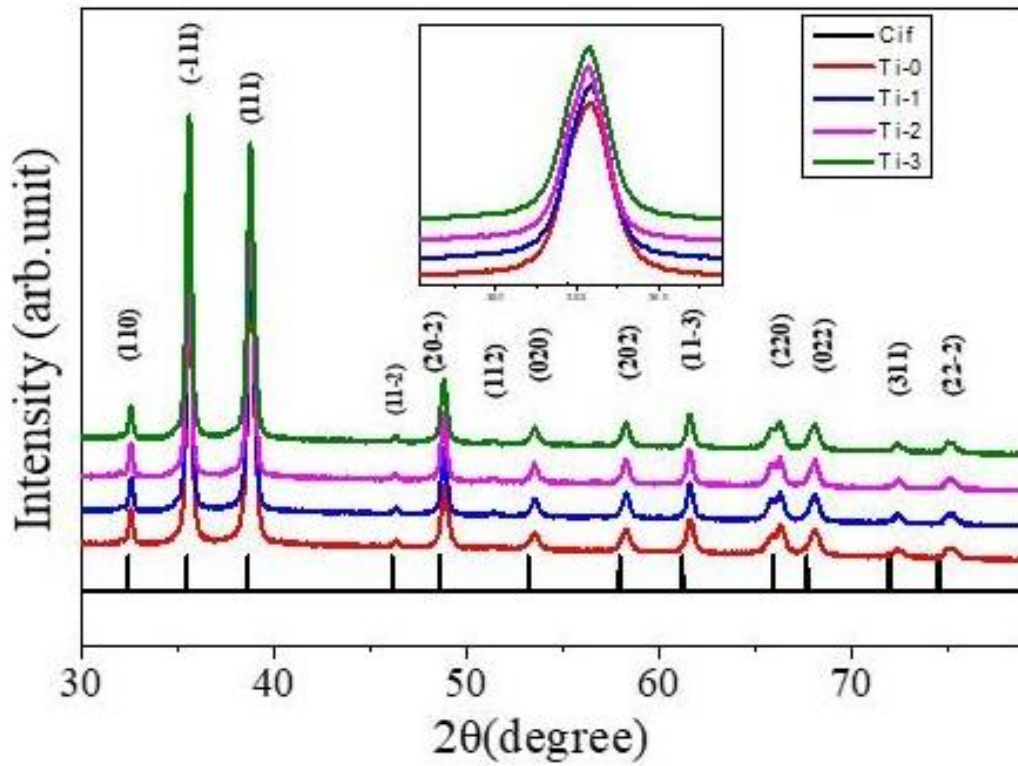


Figure 15 XRD pattern, Bond Length (unit Å), Bond angle and Lattice Parameter (unit Å) of Ti-doped CuO

Chapter 4: Optical properties of Composite CuO/Cu₂O and Fe, Ti- Doped CuO

4.1 Bandgap Analysis-

The optical band gaps are estimated from the Tauc plots of the reflection spectra obtained using a Research India UV-visible spectrophotometer. The formula used to calculate the band gap of samples using the equation:

$$\alpha h\nu = A(h\nu - E_g)^n,$$

where A is proportionality constant, E_g is the bandgap, and n is a power coefficient (where $n=1/2$ for a direct bandgap, while $n=2$ for an indirect bandgap). The literature describes an electronic direct bandgap of 2.2eV for CuO while an indirect bandgap of 1.4eV for CuO.

4.2 The Urbach Energy-

Localized states are present in between the valence band and conduction band for disordered semiconductors. Especially very close to the band edges tailing effect is observed in the density of states (DOS) due to structural disorder. These states have been detected in materials since the fifties. These band tail states are best realized in amorphous semiconductors and imperfect crystalline solids and can arise due to the thermal variation, change in the chemical composition, and any dislocation or vacancy²⁸. This DOS of these tails varies exponentially in the absorption coefficient (α) and can be estimated as an energy related to these states as Urbach energy:

$$\ln[\alpha] = \ln [\alpha_0] + (E/E_U)$$

where E_U is the Urbach energy, and α_0 is a constant. The behavior of α is referred to in the literature as Urbach-Martienssen's rule.

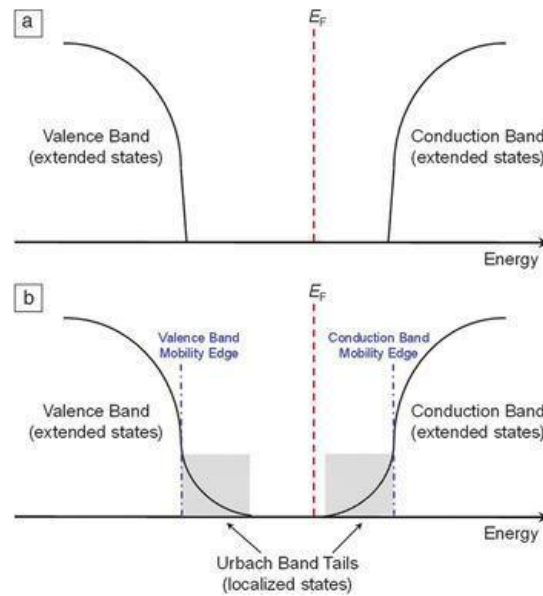


Figure 16 localized state formation in between the valance band and Conduction band.

4.3 - CuO-Cu₂O Composite

Two transitions are observed in the S500 sample, corresponding to prominent CuO and Cu₂O contributions. On the other hand, the transition state in single-phase S250 has a unique transition band-edge corresponding to a CuO

phase. In figure 17, the possible direct bandgap of composite S500 observed is between ~ 2.20 to ~ 2.80 eV. On the other hand, the direct bandgap of S250 was ~ 1.4 eV. The Composite has some transition in the indirect bandgap of the range around 2.10 eV. It means S250 has a complete direct bandgap. On the other hand, the S500 composite has both possibilities in direct and indirect bandgap transition²⁹.

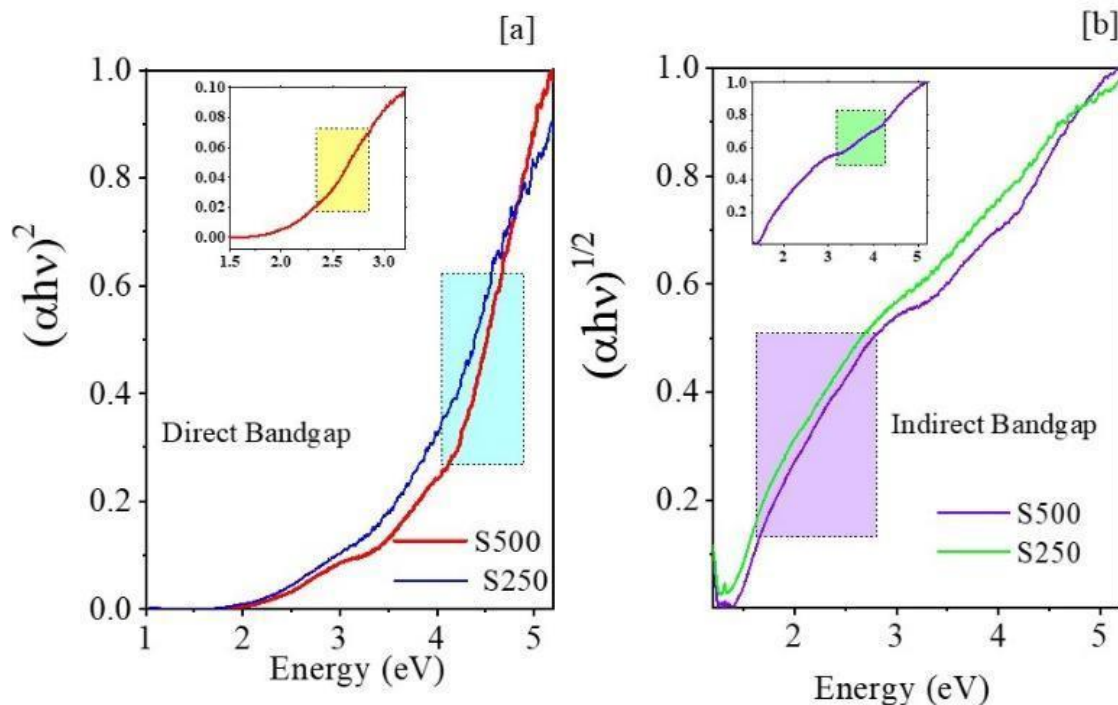


Figure 17 a Direct band Gap; b- Indirect bandgap of S250 and S500

4.4 - Fe-doped CuO

The bandgap of $\text{Cu}_{1-x}\text{Fe}_x\text{O}$ shows a blue shift³⁰ with a value of 1.45 eV, greater than pure CuO. This behavior agrees with the literature values. The representation of the variation of the bandgap of Fe-0, Fe-1, Fe-2, and Fe-3 samples with respect to the bandgap of pure CuO. The widening of the bandgap in the case of doped semiconductors is due to the blocking of the low-energy transitions by the donor electrons occupying the states at the bottom of the conduction band known as the Burstein-Moss effect. Literature suggests that with a change in compressive strain, the bandgap is modified. It is reported that with very little change in compressive strain, the bandgap increased. From the XRD result, it is observed that the bond length (Cu-O₃) along with the apical axis decreases, while there are nominal changes in the other bond lengths. Hence, there is an indication of a modification of the compressive strain along the c-axis, which hints at a possible source of modification in the bandgap. However, the E_u decreases continuously with doping from 94meV to 60meV, revealing a reduction of the lattice strain. The lattice becomes ordered and possible defects modified with Fe^{3+} doping. It is likely that Fe^{3+} introduction helps in reducing the latent oxygen defects, which could have been a source of inherent strain of the pure CuO, which reduced due to the

introduction of Fe³⁺ in the lattice. The reduction in the lattice strain can be a strong reason for the lattice to become more ordered and hence electronically have a larger bandgap from Fe-0 to Fe-3.

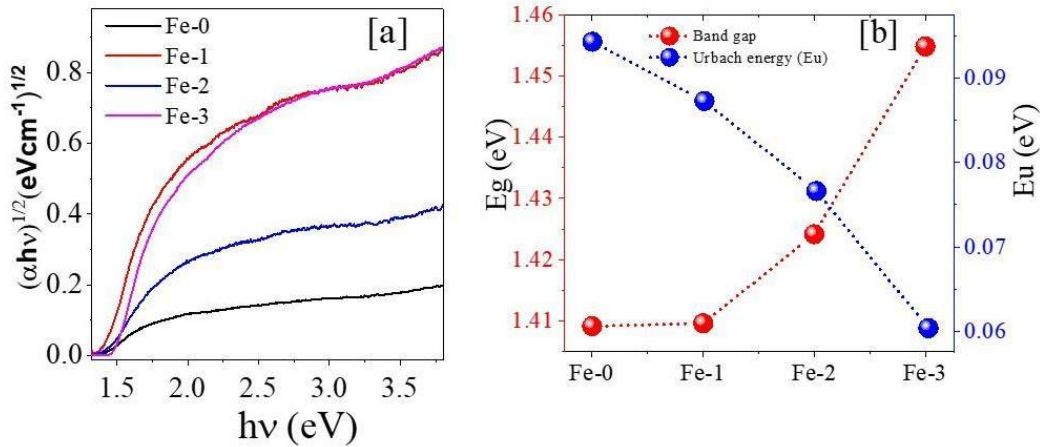


Figure 18 a- Tauc Plot, b-Band Gap and Urbach Energy of Fe Doped CuO

4.5 - Ti Doped CuO-

$\text{Cu}_{1-x}\text{Ti}_x\text{O}$ has a minimal blue shift, with values ranging from 1.415 eV in Ti-0 to 1.422 eV in Ti-1 to 1.425 eV in Ti-2, before decreasing to 1.410 eV in Ti-3³¹, as seen. This pattern is consistent with the values seen in the literature. Due to the blocking of low-energy transitions by the donor electrons occupying the states at the bottom of the conduction band, the Burstein-Moss effect causes the bandgap to increase in doped semiconductors. According to the literature, the bandgap changes when the tensile strain changes. The bandgap increased with very little change in tensile strain. The bond length (Cu-O_3) i.e., the apical axis, enlarges, as observed from the XRD analysis. This expansion modifies the tensile strain, which in turn modify may modify the bandgap. Like Fe-doping, in this case, too, the lattice may have invited more oxygen due to the larger ionic valence state of Ti^{4+} than Cu^{2+} , thereby reducing or removing the latent oxygen vacancies. This may be the reason behind a better lattice reorganization and, thereby, a change in lattice strain. The originally induced band tails in the parent CuO structure thus could have reduced, annihilating certain localized defect states (disorders, lack of crystallinity, etc.), i.e., reduction of the Urbach tail and resulted in the increase of bandgap. The E_u drops from 80 to 66 meV as substitution increases. As a result, the indirect bandgap widens, and band tails change in samples.

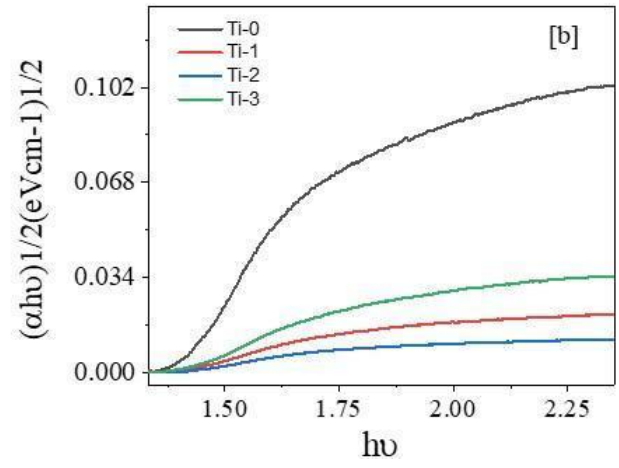
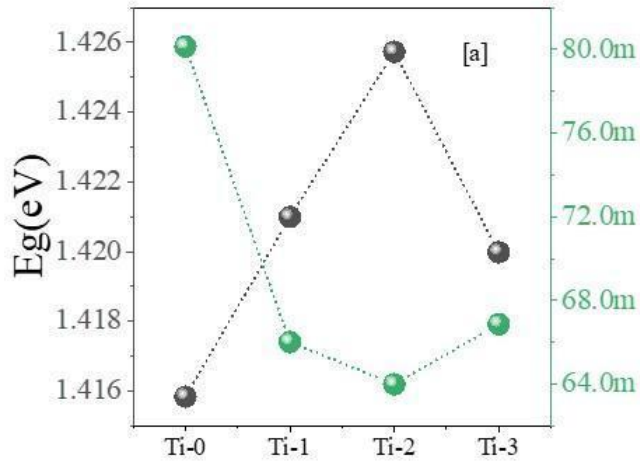


Figure 19 a- E_g , E_u plots; b- Tau Plot Of Ti doped CuO

Chapter 5-Electrical and Light sensing properties of CuO/Cu₂O and Fe, Ti doped CuO.

5.1 Proposed Model and Principle

The traditional photo-carrier generation/recombination and oxygen adsorption/desorption methods are used to operate the metal-oxide-based photodetector. The bulk surface of a CuO p-type semiconductor is electrically resistive. After electron-hole pair formation due to photoexcitation the electrons [$h\nu \rightarrow e^- + h^+$] will engage themselves in the adsorption process [$O_2 + e^- \rightarrow O_2^-$] leaving the holes behind. The hole concentration will thus build up on the surface. These holes will hence act like an electrically conductive layer on the surface. The lifetime of unpaired holes is extended, and the hole accumulation layer increases in depth. This will enable a photocurrent to be generated abruptly when light illuminates the surface.

When the light is switched off, electrons and holes swiftly recombine, and the photocurrent abruptly decreases. In addition, the remaining holes emit the ionized oxygen ions. [$h^+ + O_2^- \rightarrow O_2$]. As a result, the hole accumulation layer shrinks, contributing to the photocurrent's sluggish decay. According to the proposed model, the bandgap, defect states, and response time all have a significant impact on the dark current, photocurrent, and reaction time. The CuO's optoelectronic properties are enhanced by modifying the defect state and improving the conductivity with doping.

To investigate the actual variation in time constants and current constants, the best cycles was fitted by using the exponential growth and decay processes by using the equation: $I = I_0 + I_p \cdot \exp(-\tau/\tau_1)$; where, τ_1 is a time constant and I_0, I_p is two characteristic current constants representing a basic dark current and an additional photocurrent. Thus, the light 'ON' condition, i.e., growth current is expressed as: $I = I_0(max) - I_{g1} \exp(-\tau/\tau_{g1})$, while for light 'OFF' conditions, i.e., the decay current is expressed as: $I = I_0(min) + I_{d1} \exp(-\tau/\tau_{d1})$.

The dark current, $I_{min} \rightarrow (I_0(max) - I_{g1})$ or $I_0(min)$. On the other hand, in the presence of light the maximum current $I_{max} \rightarrow (I_0(max) + I_{d1})$ or $I_0(max)$. The sensing photocurrent, $\Delta I = (I_{max} - I_{min})$ was calculated. Thereafter, the sensitivity, $S = (\Delta I/I_{min}) * 100$, was also calculated

5.2 - UV and Visible light sensing of CuO/Cu₂O-

The photocurrent was measured under applied bias voltage of 8V as shown. Light-sensing properties of S250 and S500 samples were studied in the wavelength range of UV and visible lights for different wavelengths of 290 nm, 450 nm, 540 nm and 640 nm³². A variation in current for UV light is observed in both samples and was higher for S500. A visible light sensing was observed for S500 as well, which was weaker than the UV-response. For the S250 sample, a weaker UV-response was observed. There was no visible light response in the S250 sample. To investigate

the current variation with respect to time, four continuous cycles of samples 4 min ON and 4 min OFF conditions were applied.

Using the equation: $I = I_0 + I_p \cdot \exp(-t/\tau_1)$; the current constants and time constants of S250 and S500 were plotted for UV and visible lights. Time constants were obtained for UV lights in both samples. The variation in time-constants and current constants for both processes (growth and decay) were also shown. The parameters I_{\max} , I_{\min} , ΔI , and the sensitivity, S%, of the samples were plotted. Although the current was much higher for the S500 sample, the UV-response was faster for S250 than S500. As discussed earlier, oxygen-adsorption occurs in the presence of light. Due to lower annealing temperature of 250 °C, the possibilities of interstates or defects in the S250 sample is more than the S500 sample which was annealed at 500 °C. Higher number of defect states means higher number of trap states. Hence, the recombination rate of electrons and holes is significantly less for UV in the S500 sample. Hence, a higher current may be possible in S500.

There is a visible light sensing observed in S500 which is significantly lower than the UV-sensing. Hence the recombination of electrons and holes from defect states involving such transitions is significantly low in this sample. The drastic variation in current ΔI and Sensitivity was noted for UV light in S500 rather than S250. Literature suggests the formation energies of Cu-rich/O-poor and Cu-poor/O-rich have the lowest formation energies than other intrinsic acceptor defects in Cu_2O . The transition level of V_{Cu} is at 0.28 eV above the valence band maximum (E_V) and for V_{Cu} , split at 0.47 eV above E_V . Formation energies for both defects are very close to each other (1.15–1.14) eV and at least 0.70 eV lower than for the oxygen interstitials. The theoretical studies and reports suggest the interstates of Cu are very near to conduction in Cu_2O . Hence, the transition of these carriers may be possible from these interstates directly in S500 samples than the transition of these carriers may be possible from these interstates directly in S250 samples. In S250 indirect band gap exists, for the S500 sample, both types of bandgap were observed. The applied energy in both cases is higher than its bandgap. Hence there are possibilities of better visible light sensing than UV light sensing in both samples. However, the visible light sensing was observed in the S500 sample. On the other hand, the current variation with voltages in both samples. It means the defects state in the samples affects the visible light sensing. In the S250 sample the electrons are excited in CB with applied energies but the relaxation of electrons was not processed by the presence of such a center which is not allowing the relaxation of electrons in VB. However, in the S500 sample both CuO and Cu_2O phases are present, and there are also some defect levels that are much closer to VB such as V_{Cu} as discussed. Hence it is possible the transportation of charged excitons possibly from the defect levels such as V_{Cu} . Thus, the transportation of electrons becomes easy from these levels to VB and lower energies light were also sensed by the sample S500. It means, defects have an important role in controlling the current variation for corresponding wavelengths in visible region.

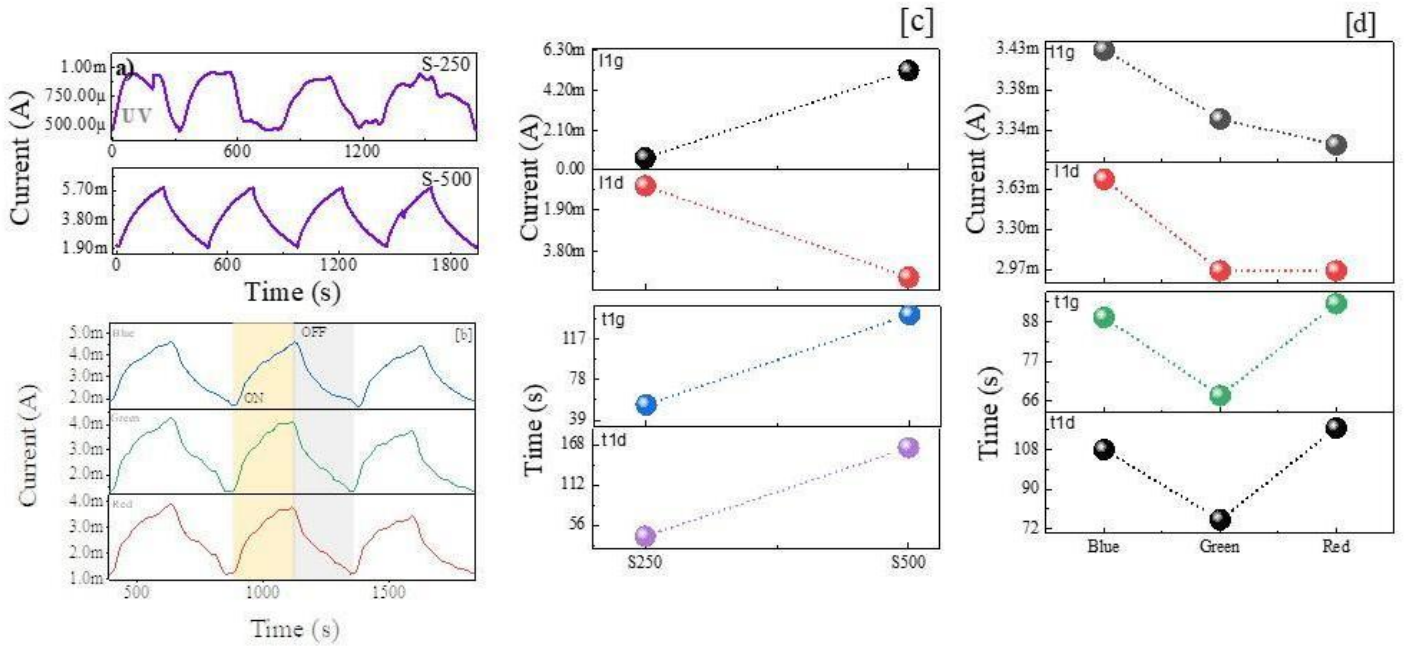


Figure 20 a-UV Sensing of S250, S500; b-Visible Sensing of S500; c- Current Constant UV; d- Time Constant UV; d- Current and Time Constant of S500 Visible Sensing

5.3 - Fe-Doped CuO-

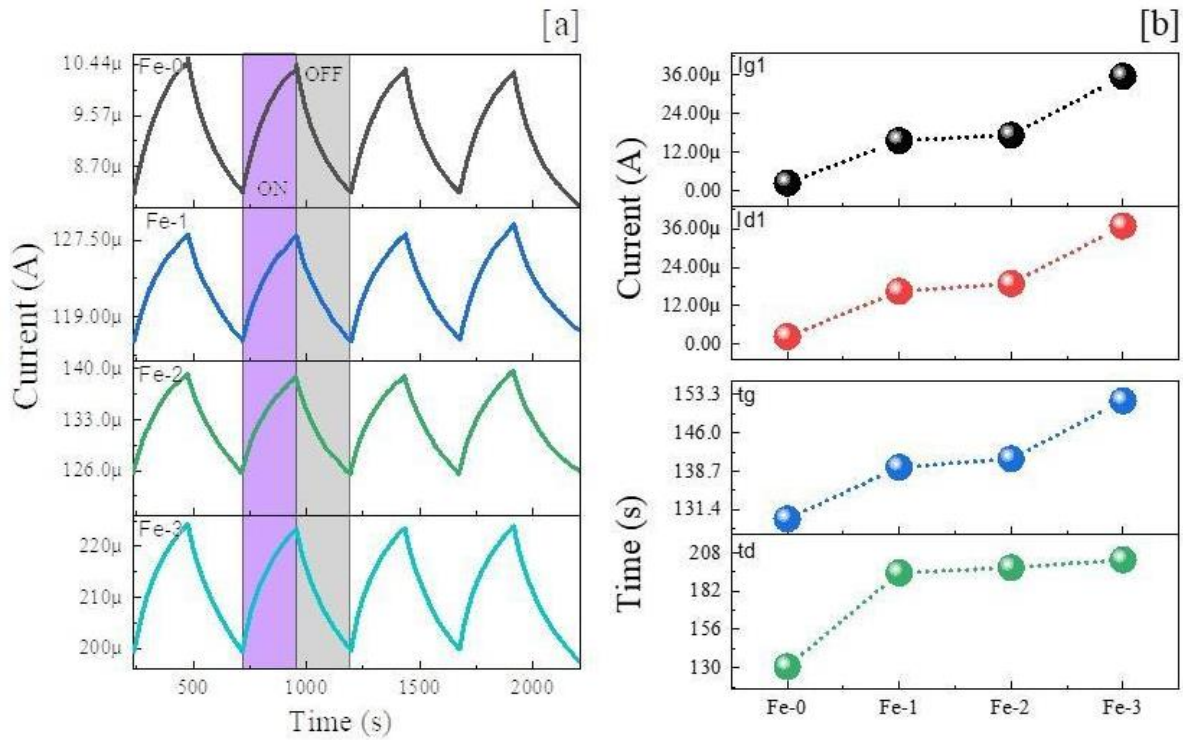


Figure 21 a-UV sensing; b- Current and Time Constant, of Fe Doped CuO

According to theoretical sources, CuO exhibits two different defects. The conductivity of V_{Cu} and O_i tends to be P-type. Furthermore, the production energies of these defects are lower and closer to those of VBM (Valence band maxima). As a result of the smaller ionic radii and higher charge, the cationic defect O_i rises with Fe doping. It implies that more oxygen is allowed into the lattice, resulting in a reduction in defects such as V_O^{33} . Despite increasing the compressive strain, the Urbach energy of the induced band tails tends to decrease. The energy of photons is sufficient to activate electrons in the conduction band in UV lighting. However, because of its p-type nature and the rise in O_i defects caused by Fe doping, the number of hole carriers in the molecule increases. The electron killer character of the O_i -level, on the other hand, tends to reduce sample sensitivity at various wavelengths. As a result, the carriers' transit is determined first by the population density of the defects center and then by the photon energy available. It suggests that the energy available for UV light sensing is much higher than the bandgap between doped and undoped materials. As a result, it helps in increasing the population density of photogenerated electrons in the VB and at the acceptor level (O_i) near or in the conduction band. As a result, UV sensitivity was reported to be increased. However, due to the leading character of dark current, it diminishes from sample to sample.

5.4 - Ti Doped CuO-

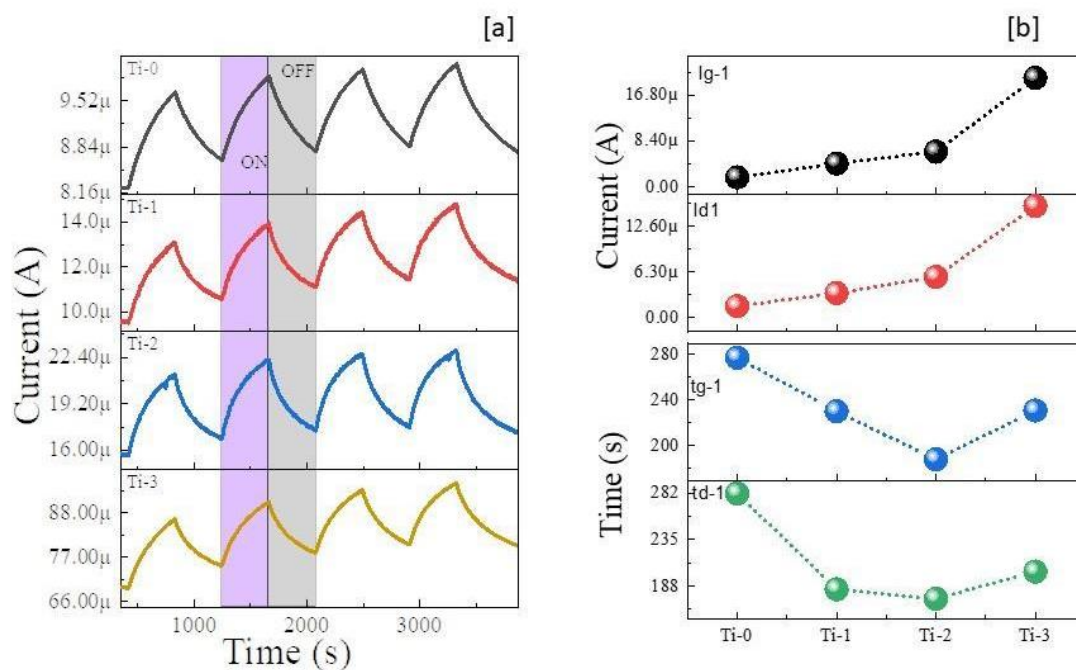


Figure 22 a-UV Sensing; b-Current and Time Constants of Ti doped CuO

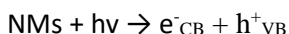
Cationic deficiency arising as a result of greater ionic radii and increased charge, possibly the O_i with increased Ti doping. It means that more oxygen can enter the lattice, reducing imperfections such as V_O . As tensile strain is raised, the Urbach energy of the induced band tails tends to decrease. Photons in the conduction band are excited by UV light because it has enough energy. In UV lighting, photon energy is sufficient to excite electrons in the conduction band. The number of hole carriers in the molecule increases due to its p-type nature and the increase in O_i defects generated by Ti doping. As a result, the carriers' transit is determined first by the defects center's population density, then by the amount of photon energy available. The energy available for UV light sensing appears to be significantly higher than the bandgap between doped and undoped materials, implying that the energy available for UV light sensing is substantially higher than the bandgap between doped and undoped materials. As a result, it aids in raising the population density of photogenerated electron hole pairs in the conduction band (CB) and at the acceptor level (O_i) near or within the conduction band. The sensitivity increased when the doping of Ti went from 13.7 % Ti-0 to 30.4 % Ti-1, then declined significantly to 29.81 % in Ti-2, and then further to 20.06 % in Ti-3. This was because of high conductivity but dark current start leading for higher doping and thus, decreased the sensitivity. Because of the more ordered lattice, the growth and decay times were radially reduced compared to the pure samples, as confirmed by the Urbach tail. In a similar fashion, the growth and decay currents rose.

Chapter 6

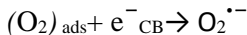
Detailed Mechanism-

Heterogeneous photocatalysis, one of the new oxidation methods or advanced oxidation processes (AOP), appears to be a developing destructive technique that leads to total mineralization of most organic contaminants, following the commonly suggested mechanism.³⁴

1-Absorption of efficient photons ($h\nu > E_G$) by the nanomaterial.



2-Oxygen ionosorption (first step of oxygen reduction; oxygen's oxidation degree passes from 0 to $-1/2$)



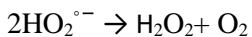
3-Neutralization of OH^- groups by photo holes which produces OH° radicals



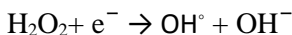
4-Neutralization of $\text{O}_2^{\circ-}$ by protons



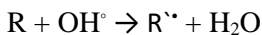
5-Transient hydrogen peroxide formation and dismutation of oxygen



6-Decomposition of H_2O_2 and second reduction of Oxygen



7-Oxidation of the organic reactant via successive attacks by OH° radicals



8- Direct oxidation by reaction with holes



The C-S+=C functional group in MB, which is in direct Coulombic interaction with the surface of Nanoparticles, can be attacked by OH radicals. As a result, the breakage of the bonds of the C-S+=C functional group in MB can be attributed to the first step of MB degradation. The transition from C-S+=C to C-S(=O)-C necessitates the preservation of the double bond conjugation, which causes the core aromatic ring containing both heteroatoms, S and N, to open. The proton reduction by photo-generation can be postulated as the source of H atoms required for C-H and N-H bond formation.

6.1 – Photocatalysis of Composite CuO/Cu₂O-

The photocatalytic property of the prepared sample was investigated using Methylene blue dye (MB) in the presence of a UV lamp (290 nm) of 11Watt placed at the distance of 10 cm from the sample. The 250mg dopant were added to the 20 mg/L of MB solution and then stirred magnetically for 30 min in dark to obtain the equilibrium of absorption/desorption of nanoparticles over the MB dye after that it is placed under the influence of UV lamp. Each time a sample of 5ml was taken out in cuvettes and then the absorption spectra was seen. The photocatalytic efficiency was calculated as C_t / C_0 ; where C_0 is the initial absorbance of the sample in the dye where C_t is the absorbance at time t after every 20 min Composite exhibit highest photocatalytic activity when compared with that of CuO. The photo-degradation efficiency of nanocomposite for methyl blue (MB) degradation was enhanced from ~12 to 31% and a sudden increase is seen at $t=180$ min. It results in the S500 sample which is composed of CuO-Cu₂O.

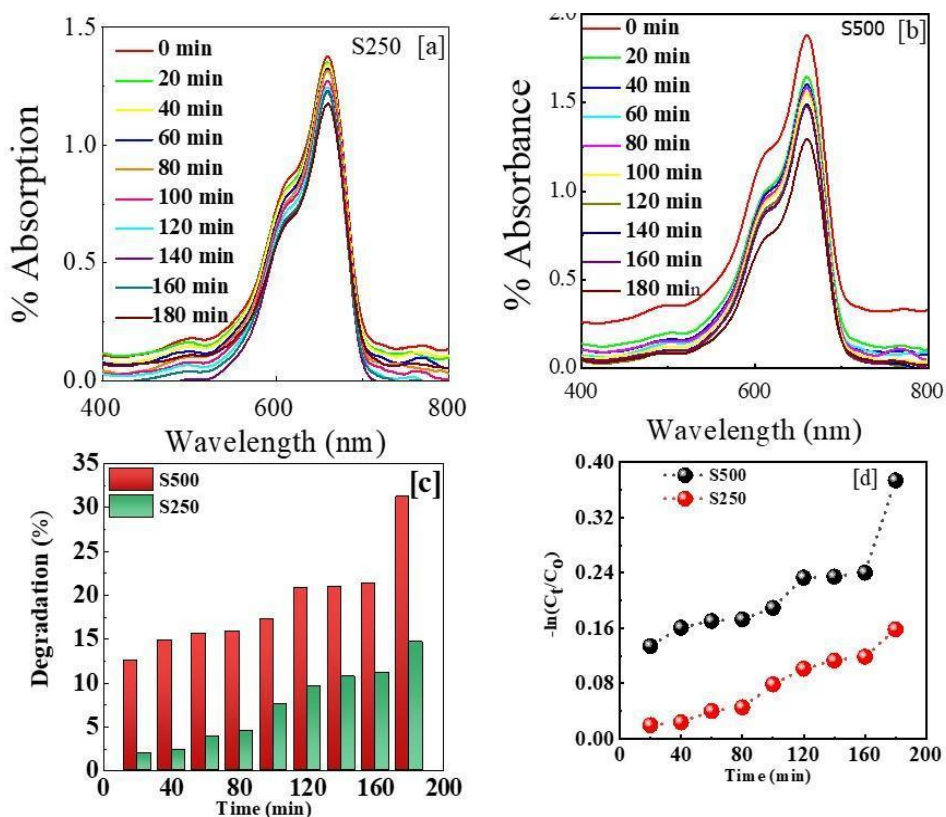


Figure 23 a- S250 absorption; b- S500 absorption; c- degradation %; d- $-\ln(C_t/C_0)$ vs Time

Chapter 7

Conclusion and future work-

XRD was used to examine the structural phase of the CuO/Cu₂O composite, as well as Fe and Ti doped CuO. The optical band gap and Urbach energy of the samples were computed and were correlated to structural characteristics such as bond lengths, lattice constants, and strain. Addition, the UV and visible light sensing of CuO/Cu₂O composite samples were examined, and due to its directive band gap nature, it showed good sensitivity in visible bands. UV sensing of Ti and Fe doped CuO was also done, and the structural defects and crystallinity of the samples were connected. CuO/Cu₂O nanoparticles were used to photo catalyze the breakdown of methylene blue dye. This suggests that nanoparticles play a vital role in the dye solution's degree.

Future Work –

- 1- It is interesting to see the defect correlated optical defect study and sensing (gas sensing, light sensing) of other metal oxides like Fe_2O_3 , NiO, ZnO etc.
- 2- To see the nanoparticle degradation and interaction with different dyes with and without the help of scavengers.
- 3- To see the application of pn Junction diodes and heterojunctions in the magnetic devices and photodetector

REFERENCE-

1. Mitra, A. & De, G. Sol-Gel Synthesis of Metal Nanoparticle Incorporated Oxide Films on Glass. in *Glass Nanocomposites* 145–163 (Elsevier, 2016). doi:10.1016/B978-0-323-39309-6.00006-7.
2. Khan, I., Saeed, K. & Khan, I. Nanoparticles: Properties, applications and toxicities. *Arabian Journal of Chemistry* **12**, 908–931 (2019).
3. Das et al. - 2017 - Biological synthesis of metallic nanoparticles pl.pdf.
4. Leong et al. - 2020 - Unified View of Magnetic Nanoparticle Separation u.pdf.
5. Weir, A., Westerhoff, P., Fabricius, L., Hristovski, K. & von Goetz, N. Titanium Dioxide Nanoparticles in Food and Personal Care Products. *Environ. Sci. Technol.* **46**, 2242–2250 (2012).
6. Rawat, A., Soni, U., Malik, R. S. & Pandey, S. C. Facile synthesis of UV blocking nano-sized Zinc Oxide and Polymethyl-methacrylate polymer nanocomposite coating material. *Nano-Structures & Nano-Objects* **16**, 371–380 (2018).
7. Niveditha, C. V., Fatima, M. J. J. & Sindhu, S. Comprehensive Interfacial Study of Potentio-Dynamically Synthesized Copper Oxide Thin Films for Photoelectrochemical Applications. *J. Electrochem. Soc.* **163**, H426–H433 (2016).
8. Siddiqui, H., Parra, M. R., Pandey, P., Qureshi, M. S. & Haque, F. Z. Utility of copper oxide nanoparticles (CuO-NPs) as efficient electron donor material in bulk-heterojunction solar cells with enhanced power conversion efficiency. *Journal of Science: Advanced Materials and Devices* **5**, 104–110 (2020).
9. Ghijssen, J. *et al.* Electronic structure of Cu₂O and CuO. *Phys. Rev. B* **38**, 11322–11330 (1988).
10. Önsten, A., Göthelid, M. & Karlsson, U. O. Atomic structure of Cu₂O(111). *Surface Science* **603**, 257–264 (2009).
11. Yang, M., He, J., Hu, X., Yan, C. & Cheng, Z. CuO Nanostructures As Quartz Crystal Microbalance Sensing Layers for Detection of Trace Hydrogen Cyanide Gas. *Environ. Sci. Technol.* **45**, 6088–6094 (2011).
12. Zoolfakar, A. S., Rani, R. A., Morfa, A. J., O’Mullane, A. P. & Kalantar-zadeh, K. Nanostructured copper oxide semiconductors: a perspective on materials, synthesis methods and applications. *J. Mater. Chem. C* **2**, 5247–5270 (2014).
13. Jung, T. S. *et al.* Enhancement of Switching Characteristic for p-Type Oxide Semiconductors Using Hypochlorous Acid. *ACS Appl. Mater. Interfaces* **10**, 32337–32343 (2018).
14. Djurišić, A. B., He, Y. & Ng, A. M. C. Visible-light photocatalysts: Prospects and challenges. *APL Materials* **8**, 030903 (2020).
15. Dasineh Khiavi, N. *et al.* Visible Light Driven Heterojunction Photocatalyst of CuO–Cu₂O Thin Films for Photocatalytic Degradation of Organic Pollutants. *Nanomaterials* **9**, 1011 (2019).

16. Li, J. & Wu, N. Semiconductor-based photocatalysts and photoelectrochemical cells for solar fuel generation: a review. *Catal. Sci. Technol.* **5**, 1360–1384 (2015).
17. Du, Y., Meng, X. & Gao, X. Variations of the microstructure and the optical and electrical properties with sputtering power for direct-current-magnetron-sputtered indium-doped CuO thin films at room temperature. *Thin Solid Films* **684**, 53–58 (2019).
18. Shaikh, J. S. *et al.* Synthesis and characterization of Ru doped CuO thin films for supercapacitor based on Bronsted acidic ionic liquid. *Electrochimica Acta* **56**, 2127–2134 (2011).
19. Gao, W., Yang, S., Yang, S., Lv, L. & Du, Y. Synthesis and magnetic properties of Mn doped CuO nanowires. *Physics Letters A* **375**, 180–182 (2010).
20. Chand, P., Gaur, A., Kumar, A. & Kumar Gaur, U. Structural and optical study of Li doped CuO thin films on Si (100) substrate deposited by pulsed laser deposition. *Applied Surface Science* **307**, 280–286 (2014).
21. Li, Y. *et al.* Structural and room-temperature ferromagnetic properties of Fe-doped CuO nanocrystals. *Journal of Applied Physics* **107**, 113908 (2010).
22. Ward, D. A. & Ko, E. I. Preparing Catalytic Materials by the Sol-Gel Method. *Ind. Eng. Chem. Res.* **34**, 421–433 (1995).
23. Zaitoun, M. A. & Lin, C. T. Chelating Behavior between Metal Ions and EDTA in Sol–Gel Matrix. *J. Phys. Chem. B* **101**, 1857–1860 (1997).
24. Chai, C. Critical ageing of hydroxyapatite sol–gel solutions. *Biomaterials* **19**, 2291–2296 (1998).
25. Zayyoun, N., Bahmad, L., Laânab, L. & Jaber, B. The effect of pH on the synthesis of stable Cu₂O/CuO nanoparticles by sol–gel method in a glycolic medium. *Appl. Phys. A* **122**, 488 (2016).
26. Oliveira, A. A., Valerio-Cuadros, M. I., Tupan, L. F. S., Ivashita, F. F. & Paesano, A. Size-effect on the optical behavior of Fe-doped CuO nanoparticles synthesized by a freeze-drying process. *Materials Letters* **229**, 327–330 (2018).
27. Masudy-Panah, S. *et al.* Titanium doped cupric oxide for photovoltaic application. *Solar Energy Materials and Solar Cells* **140**, 266–274 (2015).
28. Usha, V., Kalyanaraman, S., Thangavel, R. & Vettumperumal, R. Effect of catalysts on the synthesis of CuO nanoparticles: Structural and optical properties by sol–gel method. *Superlattices and Microstructures* **86**, 203–210 (2015).
29. Mosleh, S., Rahimi, M. R., Ghaedi, M., Dashtian, K. & Hajati, S. Sonochemical-assisted synthesis of CuO/Cu₂O/Cu nanoparticles as efficient photocatalyst for simultaneous degradation of pollutant dyes in rotating packed bed reactor: LED illumination and central composite design optimization. *Ultrasonics Sonochemistry* **40**, 601–610 (2018).
30. Iqbal et al. - 2019 - Synthesis and characterization of transition metal.pdf.

31. Iqbal, M. *et al.* Synthesis and characterization of transition metals doped CuO nanostructure and their application in hybrid bulk heterojunction solar cells. *SN Appl. Sci.* **1**, 647 (2019).
32. Song, H.-J. *et al.* High-Performance Copper Oxide Visible-Light Photodetector via Grain-Structure Model. *Sci Rep* **9**, 7334 (2019).
33. Chen, H. *et al.* A copper-based sorbent with oxygen-vacancy defects from mechanochemical reduction for carbon disulfide absorption. *J. Mater. Chem. A* **4**, 17207–17214 (2016).
34. Akter, J. *et al.* Kinetically controlled selective synthesis of Cu₂O and CuO nanoparticles toward enhanced degradation of methylene blue using ultraviolet and sun light. *Materials Science in Semiconductor Processing* **123**, 105570 (2021).